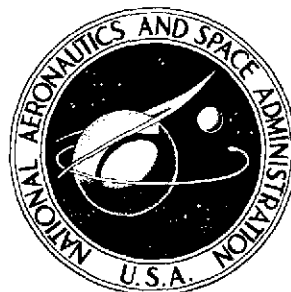


**NASA TECHNICAL
MEMORANDUM**



NASA TM X-3158

NASA TM X-3158

(NASA-TM-X-3158) EXPERIMENTAL AND
ANALYTICAL STUDY OF AN INLET FOREBODY FOR AN
AIRFRAME-INTEGRATED SCRAMJET CONCEPT (NASA)
60 p HC \$4.25 CSCL 01B

N75-14709

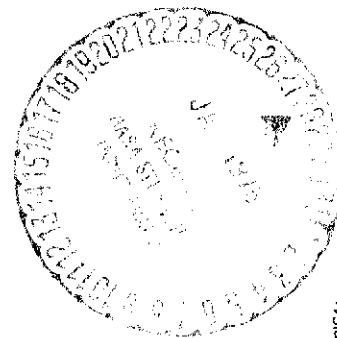
Unclass

H1/01 07820

**EXPERIMENTAL AND ANALYTICAL
STUDY OF AN INLET FOREBODY FOR
AN AIRFRAME-INTEGRATED SCRAMJET CONCEPT**

*Earl H. Andrews, Jr., Anthony M. Agnone,
and S. Z. Pinckney*

*Langley Research Center
Hampton, Va. 23665*



1. Report No. NASA TM X-3158		2. Government Accession No.		3. Recipient's Catalog No.	
4. Title and Subtitle EXPERIMENTAL AND ANALYTICAL STUDY OF AN INLET FOREBODY FOR AN AIRFRAME-INTEGRATED SCRAMJET CONCEPT				5. Report Date January 1975	
				6. Performing Organization Code	
7. Author(s) Earl H. Andrews, Jr., Anthony M. Agnone, and S. Z. Pinckney				8. Performing Organization Report No. L-9836	
9. Performing Organization Name and Address NASA Langley Research Center Hampton, Va. 23665				10. Work Unit No. 505-05-41-01	
				11. Contract or Grant No.	
12. Sponsoring Agency Name and Address National Aeronautics and Space Administration Washington, D.C. 20546				13. Type of Report and Period Covered Technical Memorandum	
				14. Sponsoring Agency Code	
15. Supplementary Notes Anthony M. Agnone is Senior Research Scientist, New York University Aerospace Laboratory.					
16. Abstract <p>Preliminary analytical and experimental inlet forebody investigations have been conducted at Mach numbers of 6.0 and 8.5 in a cooperative effort between the National Aeronautics and Space Administration and the New York University School of Engineering and Science under a grant directed by Dr. A. Ferri. The forebody design concept consisted of a sharp-nosed right circular cone followed by elliptical cross sections. This concept resulted in swept isentropic compression which would allow swept cowl leading edges.</p> <p>Measurements were made to define the condition of the inviscid flow field developed by the forebody, including flow profiles in the vicinity of cowl leading-edge stations, and the three-dimensional boundary-layer effects. The investigation verified some of the expected differences between the predicted and the experimental results.</p>					
17. Key Words (Suggested by Author(s)) Inlets Fluid dynamics (inviscid and viscous) Method of characteristics				18. Distribution Statement Unclassified - Unlimited STAR Category 01	
19. Security Classif. (of this report) Unclassified.	20. Security Classif. (of this page) Unclassified	21. No. of Pages 58	22. Price* \$4.25		

EXPERIMENTAL AND ANALYTICAL STUDY OF AN INLET FOREBODY FOR AN AIRFRAME-INTEGRATED SCRAMJET CONCEPT

By Earl H. Andrews, Jr., Anthony M. Agnone,*
and S. Z. Pinckney
Langley Research Center

SUMMARY

A preliminary analytical and experimental investigation has been conducted for a vehicle inlet forebody that was designed to have elliptical cross sections downstream of an initial sharp-nosed right circular cone. This concept resulted in the isentropic portion of the compression being performed in a swept manner. The investigations were conducted at Mach 6.0 and 8.5.

Inviscid flow-field analytical results were obtained by two different methods; one used a method of near characteristics and the other used a finite-difference solution to the unified supersonic/hypersonic small-disturbance equations. Longitudinal pressure distributions were well predicted by both methods. An integrodifferential boundary-layer method predicted no-trip boundary-layer thickness parameters within 10 to 20 percent. Effects of boundary-layer cross flow from the major-axis plane to the minor-axis plane because of the body contour were noted for 0° angle of attack. At 5° angle of attack with the windward side in the minor-axis plane, the results were too inconclusive to ascertain a boundary-layer cross-flow trend. The results of this investigation indicated that the original location of the inlet cowl should be reconsidered.

INTRODUCTION

Most studies in the literature on hypersonic air-breathing cruise or accelerating vehicles assume that the propulsion system and airframe are highly integrated in order to provide the maximum potential performance. A research program directed at the development of concepts for supersonic combustion ramjets (scramjets) is in progress at NASA Langley Research Center. The goal of this program is to develop technology required to design such airframe-integrated propulsion systems. This hypersonic propulsion program has been discussed in several papers (refs. 1 to 5).

*Senior Research Scientist, New York University Aerospace Laboratory.

One segment of the Langley propulsion program is a cooperative effort between NASA and the New York University School of Engineering and Science under a grant directed by Dr. A. Ferri (NASA Grant NGR 33-016-131). References 6 to 18 report on part of the work accomplished under the grant. The major portion of this cooperative effort is directed at research on a concept for an integrated thermal compression scramjet. The concept employs the vehicle forebody for inlet external compression. A conical nose forms the initial portion of the forebody followed by isentropic compression surfaces that form forebody elliptical cross sections. A forebody so designed results in the compression surface terminating in a swept plane; this allows the inlet cowl leading edge to be swept in a circumferential direction. Swept cowl leading edges provide a capability for spilling flow during the inlet starting process and are advantageous in alleviating the high heating rates of sharp leading edges.

The flow field for such highly integrated configurations must be determined as accurately as possible since the magnitude and direction of the propulsion forces (ram, spillage, gross thrust, etc.) can significantly influence the trim requirements of the complete vehicle configuration. Wind-tunnel sizes are limited and flight Reynolds number simulation is not possible; therefore, theoretical predictions must be relied upon more heavily in these configurations than in conventional vehicles. The basic analytical prediction method used by the New York University team for their design is described in reference 7. The method was not exact in that it assumed irrotational flow; therefore, verification of some of the expected differences between the predicted and the experimental results, especially at angles of attack, was a primary goal of this study.

The present investigation was initiated to specifically measure the conditions of the inviscid flow field developed by the forebody, including flow profiles in the vicinity of the cowl leading-edge station, and the three-dimensional boundary-layer effects. The design concept generates cross flows in the boundary layer to drive the low momentum fluid in the viscous layer into regions of low pressure gradients to prevent boundary-layer separation; an evaluation of the magnitude of these effects was desired, including the effect of angle of attack.

In order to study these various effects and to obtain experimental data for comparison with the analytical method employed, an inlet forebody model was fabricated and experimentally investigated in the Langley 20-inch hypersonic tunnels at free-stream Mach numbers of 6.0 and 8.5. Reynolds number per meter for both Mach numbers was 1.476×10^7 and the model wall temperature was near adiabatic wall temperature. The model was tested with and without boundary-layer trips installed and at angles of attack from 0° to 5° . The model scale was about 1/210 the size of a typical vehicle. Experimental data results are presented in the form of pressure distributions (ratio of surface

static pressure to free-stream total pressure), survey pitot pressure profiles, boundary-layer thickness parameters, schlieren photographs, and oil flow patterns.

SYMBOLS

a	major axis of an ellipse
b	minor axis of an ellipse
l	length of model (40.64 cm)
M	Mach number
M_ℓ	local Mach number
P_{pitot}	pitot pressure, atm ($1 \text{ atm} = 1.013 \times 10^5 \text{ N/m}^2$)
P_s	surface static pressure, atm
$P_{t,\infty}$	free-stream total pressure, atm
R	Reynolds number per meter
r	radius perpendicular to model center line, cm
T	static temperature, K
$T_{t,\infty}$	free-stream total temperature, K
u	velocity, m/sec
x	longitudinal distance from nose vertex, cm
y	distance from model surface, perpendicular to model surface, cm
y'	distance from reference plane to center line of probes on Mach 8.5 multiple probe survey rake (see fig. 4(b)), cm
z	ratio of the distance of survey probe center line from model surface to maximum (2.54 cm) survey distance, perpendicular to tunnel center line

α	angle of attack, deg
δ	boundary-layer velocity thickness, cm
δ^*	boundary-layer displacement thickness, cm
ϵ	angle between vertical plane and shaft of multiple probe survey rake (see fig. 4(b)), deg
θ	boundary-layer momentum thickness, cm
ξ	body surface angle, deg
ρ	density, g/m ³
τ	angle of reference plane to each probe of multiple probe survey rake (see fig. 4(b)), deg
ϕ	model radial planes, deg (see figs. 1(a) and 2(a))

Subscripts:

δ	boundary-layer edge
∞	free stream

APPARATUS AND PROCEDURE

Facilities and Test Conditions

The Mach 8.5 and the Mach 6.0 tunnels employed in this investigation are briefly described in reference 19. The Mach 8.5 tunnel is a blowdown type facility that employs an axisymmetric contoured nozzle with a 53.3-cm-diameter (21-in.) test section; the test core is about 40.6 cm (16 in.) in diameter. The Mach 6.0 tunnel is also a blowdown type facility, but a two-dimensional contoured nozzle is employed with a 50.8-cm (20-in.) square test section; the test core is about 40.6 cm (16 in.) square. An appendix of reference 20 describes in more detail the Mach 6.0 facility. The flow conditions for the experiments are listed in table 1. Tests were conducted at Reynolds numbers per meter of 0.984×10^7 , 1.476×10^7 , and 1.969×10^7 for Mach 6.0 and 1.476×10^7 for Mach 8.5; the majority of the Mach 6.0 data was obtained at 1.476×10^7 . Runs were made with

and without boundary-layer trips installed on the center body. The model wall temperature was near adiabatic. The free-stream Mach numbers were 6.0 and 8.5 with a variation of ± 0.02 . Both facilities had the capability for testing at angles of attack; tests were conducted at 0° to 5° angle of attack. All angle-of-attack tests had the $0^\circ \phi$ -plane as the windward side except for one pitot survey test at $M_\infty = 8.5$ and $\alpha = 5^\circ$ in which the $90^\circ \phi$ -plane was the windward side. Pitot pressure surveys were conducted at 0° and 5° angle of attack (see table 1). Surface static pressures were measured over the range of angle of attack from 0° to 5° in 1° increments for Mach 6.0 with and without boundary-layer trips and for Mach 8.5 with trips installed. For Mach 8.5 without trips installed, static pressure measurements were obtained for 0° and 2° angle of attack only.

Model

Design concept. - The design concept derived in the joint NASA-NYU program is shown in the schematic of figure 1. The centerbody nose is a 7.5° half-angle cone and is terminated by an oblique planar cut. This planar cut establishes a swept line, as shown in the side view, which marks the end of the initial cone surface and the beginning of the isentropic compression surface. The same amount of isentropic compression is employed in all radial planes, resulting in elliptical-shaped cross sections. The focal point of the waves emanating from the compression surfaces was chosen sufficiently downstream so as to avoid wave coalescence at Mach numbers below 8.5. After 8.5° of isentropic compression (surface slope of 16°), the compression terminates in a swept plane as shown in figure 1(a). This swept compression concept generates, at 0° angle of attack, the greatest surface pressures in the major-axis plane (ϕ of 90° , see figs. 1(a) and 2(a) for definition of ϕ or radial planes) at any axial station up to the end of the compression in the major-axis plane. The forebody boundary layer along the major-axis plane generally is driven toward the minor-axis plane ($\phi = 0^\circ$). The two inlet cowls, therefore, would be located circumferentially between the ϕ -planes of 45° to 90° and between 315° to 270° as shown in figure 1(a). The cowl leading edge corresponds to the intersection of the conical bow shock generated by the 7.5° half-angle cone at Mach 8.0 and a plane inclined 55° to the center line; that is, the cowl leading edge in the side view is swept 55° . The leading edge of the cowl in the $90^\circ \phi$ -plane (point C in fig. 1(a)) corresponds to the point of intersection of the conical bow shock at Mach 8.0 and the corresponding characteristic line emanating from the point of initial isentropic compression in that plane. Leading edges of the sidewalls located in the ϕ -planes of 45° and 315° are designed to be swept 45° relative to the vehicle axis. The internal surface of each sidewall is canted 10° outward to avoid formation of shocks due to the outward component of velocity produced by the sweep of the cowl leading edge.

The present investigation is not concerned with the nozzle; however, it is of interest to note the general design approach. At the end of the isentropic compression, the sur-

face slope of 16° remains constant for a short distance in each radial plane before the body contour turns toward the center line to simulate a nozzle surface. This type of design results in a rotation of 90° of the major and minor axes of the elliptical cross sections as indicated by the A-A and B-B cross sections in figure 1(a).

Another note of interest about this design concept is that it employs thermal compression. Thermal compression is discussed briefly in reference 3, the basic fluid dynamics of the process are described in reference 21, and reference 22 summarizes some past work on thermal-compression research engines. In the thermal-compression process, combustion-induced compression waves originating at one fuel injector are used advantageously to compress the airflow approaching injectors located in regions of low inlet contraction ratio. In order to employ thermal compression in the NASA-NYU concept, fuel-injector bodies are envisioned to be located as illustrated in figure 1(b). The thermal compression feature has several potential advantages; its dominant feature, however, is increased performance for three-dimensional fixed geometry configurations which must be limited to modest inlet geometric contraction ratios because of inlet starting requirements at low supersonic Mach numbers ($M \approx 3$).

Experimental model. - The experimental model consisted of the centerbody design with symmetric elliptical cross sections without a cowl as illustrated in figure 2. The model scale is about 1/210 of a typical vehicle 85.5 m long. Design coordinates in the 0° and 90° ϕ -planes were defined by the equations listed in table 2. Coordinates of the fabricated model were slightly different than designed; body coordinate measurements were obtained and are listed in table 3. The measured radii values of the major and minor axes are presented in figure 3(a). The centerbody surface angles in the ϕ -planes of 0° , 45° , and 90° were determined graphically by a mirror tangent method. The results are presented in figure 3(b), and the values represented by the faired curves were used to predict the flow field with the modified near-characteristics-method computer program described in references 7 and 8. The conical nose of the model has an average half-angle of about 7.25° instead of the design value of 7.5° . Also, the ϕ -plane of 45° had less than the design value of compression; a nearly straight line segment was present in the region of $0.625 \leq \frac{x}{l} \leq 0.813$ that resulted in a total compression of about 13° instead of 16° .

Since the present test conditions result in an occurrence of natural boundary-layer transition at an axial station of about 23 cm for $M_\infty = 6.0$, or midway along the compression ramp, boundary-layer trips were installed as shown in figure 2(a) to insure the existence of a turbulent boundary layer along most of the model surface. The boundary-layer trips consisted of spheres of 0.794 mm in diameter, which is approximately equal to boundary-layer thickness at the trip station; they were spot welded approximately 4.0 diameters apart (center to center) on a 0.076-mm-thick steel band. The band was conical in shape and was located at the 7.62-cm station ($x/l = 0.188$).

Flow Visualization Techniques

Schlieren. - During all the Mach 6.0 and 8.5 tests the forebody flow was viewed by parallel light schlieren systems. The results were recorded by photographic means.

Oil flows. - Flow visualization was also performed by means of oil flow tests for Mach 6.0 with and without boundary-layer trips installed. The tests were performed at 0° and 5° angles of attack. Dots of an oil-lamp black mixture were applied to the model; and after the tunnel flow was stabilized, the model was injected into the tunnel free stream for several seconds and then retracted. Photographs were used to record the flow patterns on the model. Satisfactory oil flow tests could not be conducted in the Mach 8.5 facility at the time of the tests.

Instrumentation

Experimental measurements consisted of surface static pressures, pitot pressure surveys, and free-stream total pressure and temperature. Static pressure orifices were installed in three radial planes (ϕ of 0° , 45° , and 90°); the locations are tabulated in table 4. Pitot pressure surveys were obtained with two different survey rakes that are illustrated in figure 4. A single probe rake (fig. 4(a)) was used during the Mach 6.0 tests. Because of limited run time in the Mach 8.5 tunnel, a multiple probe rake (fig. 4(b)) was used to reduce survey traverse time. The size of each probe and the distance from a reference plane to each probe center line are indicated in the table in figure 4(b). Between runs the rake shaft was bent in order to allow probe tip contact with the model surface. The angle between the bent shaft and the vertical plane, ϵ , is defined in figure 4(b) and the values of ϵ are tabulated in the last column of table 1. The surveys were conducted in such a manner that in many cases data from adjacent tubes overlapped; in such cases the data for analysis were selected from tubes which were more accurately aligned with the local flow. Flow-direction values used in the decision as to which measurement to use were estimated from the computed flow-field conditions obtained with the computer program of references 7 and 8.

Analytical Computations

Inviscid flow. - The inviscid flow field was analyzed with the aid of two different three-dimensional flow-field analysis computer programs. Comparisons were made of these two programs in terms of the accuracy, speed, and ease of computations. The first method is referred to as the method of near characteristics (refs. 7 and 8), while the second method used a finite-difference solution to the unified supersonic/hypersonic small-disturbance equations (refs. 23 and 24). These methods are discussed in appendix A.

The model surface contour was corrected for the boundary-layer displacement thickness for use in the near-characteristics method only. The corrected contour was obtained iteratively by using the near-characteristics-method program and the boundary-layer program referred to in the next section.

Viscous flow. - The viscous flow field was analyzed with the aid of an integrodifferential boundary-layer method that is somewhat more complex than that described in reference 25. A brief discussion of this prediction method is contained in appendix B.

RESULTS AND DISCUSSION

Results from the Mach 6.0 and 8.5 experimental investigations have been analyzed and are discussed in the following paragraphs. Experimental data were obtained over a range of Reynolds numbers at Mach 6.0 as stated previously in the section entitled "Apparatus and Procedure." Reynolds number variations did not, however, have a significant effect on the data results; therefore, all the data results presented are for a Reynolds number per meter of 1.476×10^7 .

Shock Correlations

Enlargements of schlieren photographs presented in appendix C were used to measure coordinates of the bow shock. These measurements are presented as the symbol points in figures 5(a) and 5(b) for Mach 6.0 and 8.5, respectively. All the experimental measurements of shock position presented are with boundary-layer trips since measurements without trips were not noticeably different. Curves are also shown representing the theoretical bow-shock locations that were obtained from the near-characteristics method. Favorable agreement between theory and experiment is noted in figure 5(a) for all three planes at Mach 6.0 for both 0° and 5° angle of attack. At Mach 8.5 the data lie above the theory by about 10 percent.

The bow (conical) shock should be straight (shock angle is 12.1° at $M_\infty = 6.0$ and $\alpha = 0^\circ$) up to the intersection point of the initial compression from the isentropic surface. The compression waves from the isentropic compression contour interact with the bow shock, and the shock slope is increased from an angle of 12.1° to 20.1° for Mach 6 and $\alpha = 0^\circ$. The corresponding flow direction is approximately 12.5° which is consistent with the conical shock strength, whose flow deviation is 3.9° behind the 12.1° shock, and the 8° to 9° change in body slope. Similarly, the bow shock for Mach 8.5 and $\alpha = 0^\circ$ has an initial slope of 10.4° that is increased to about 15.3° because of the compression waves interacting with the bow shock.

At $M_\infty = 8.5$ and $\alpha = 5^\circ$ the bow shock exhibits a "bulge" in the region $0.2 < \frac{x}{l} < 0.5$. Initially the shock angle is steeper than the theoretical conical value of

9.85°; then it becomes shallower. This effect is due to the interaction of the shock generated by the trips with the conical bow shock.

Static Pressure Distributions

Effects of swept compression.- Swept compression in the present design was obtained, as discussed in the design-concept section, by initiating the compression in the ϕ -planes of 90° and 270° and delaying the start of compression about the circumference of the body as the 0° ϕ -plane is approached from these two planes. Surface pressure distributions of this design concept were predicted by using the theoretical method of references 7 and 8. This method indicated that, at any station in the compression region up to the end of compression in the 90° ϕ -plane ($x/l \leq 0.719$), the surface pressure is greatest in the 90° ϕ -plane at 0° angle of attack; these results are shown in figures 6(a) and 6(c). Static pressure measurements obtained in the three radial planes ($\phi = 0^\circ, 45^\circ$, and 90°) are also presented in figures 6(a) and 6(b) for Mach 6.0 and figures 6(c) and 6(d) for 8.5. Good agreement was obtained between the experimental and theoretical pressure distributions for both Mach 6.0 and 8.5 at 0° angle of attack as is evident in figures 6(a) and 6(c), respectively. At Mach 6 and 5° angle of attack, figure 6(b), the agreement is not as favorable; the theory underpredicted the pressures in the 90° ϕ -plane and also underpredicted the pressures in the 0° ϕ -plane for x/l values greater than 0.80 but did predict the pressures in the 45° ϕ -plane. Possible contributions to the underpredictions are inadequacies in the computer-program input data, the assumption of irrotational flow, and/or boundary-layer cross flow. No computational results were obtained for Mach 8.5 at 5° angle of attack, figure 6(d). In general, the static-pressure trends, especially at 0° angle of attack, correspond to the trends indicated by the surface slope curves of figure 3(b). At 5° angle of attack the pressures in the 0° ϕ -plane (windward plane) at x/l of 0.719 are slightly greater than those in the 90° ϕ -plane.

With the greater pressures at x/l of 0.719 in the 90° ϕ -plane at 0° angle of attack, boundary-layer cross flow from the 90° ϕ -plane to the 0° ϕ -plane would be expected; this cross flow would have passed through the region between the split halves of the cowl design concept (see fig. 1(a)). The slightly different pressure levels at x/l of 0.719 for 5° angle of attack resulted in an inconclusive cross-flow trend. Oil flow tests, however, indicated only small amounts of cross flow occurred toward $\phi = 0^\circ$ at 0° angle of attack, but at 5° angle of attack a larger amount of cross flow was indicated to flow toward the 90° and 270° ϕ -planes from the 0° ϕ -plane. Photographs and interpretation of the oil flow tests are included in appendix D. The surface static pressure and oil flow results suggest that the two inlet cowls be combined into one cowl symmetric about the major-axis plane compression ramp and located on the lower quadrant of the vehicle forebody. (This is discussed further in the section entitled "Engine Cowl Location.")

Comparison of theoretical methods. - The theory of references 7 and 8 was used in the design of the centerbody swept compression concept and in the prediction of the surface static pressure distributions. During the course of this investigation, a fully three-dimensional theoretical method (refs. 23 and 24) became available and was used for limited comparison as shown in figure 7 for Mach 6.0. Experimental data are shown for boundary-layer trips installed in figure 7(a) and for no trips in figure 7(b). Since both computer programs are for inviscid flow, neither computer program accounts for the trips; therefore, the theoretical curves of figures 7(a) and 7(b) are the same. In general, the theory of references 23 and 24, referred to as the small-disturbance theory, follows the detailed irregularities in the data curves much more closely than the near-characteristics theory of references 7 and 8. Some difficulty was experienced in using the small-disturbance theory to match the data trend in the nearly constant-slope region of the $45^\circ \phi$ -plane, particularly at 5° angle of attack. This condition occurred because the computer generated the body contours in all planes without any longitudinal slope control except for the radii in the major and minor axes (0° and $90^\circ \phi$ -planes) which were specified by input data. There does not seem to be an inherent advantage of one of the theories over the other because the input requirements and computational times of the two programs are comparable. The differences shown are the result of the way the user specifies the input and defines the body contours.

Effect of angle of attack and boundary-layer trips. - Experimental static pressure distributions for angles of attack ranging from 0° to 5° are presented in figures 8(a) and 8(b) for Mach numbers of 6.0 and 8.5, respectively. No significant effects of the trips on the static pressure distributions are noted because the trips were located well upstream of the measurement stations. The effect of angle of attack was largest in the $0^\circ \phi$ -plane and negligible in the $90^\circ \phi$ -plane. For the $0^\circ \phi$ -plane the increase in static pressure is about 11 percent per degree angle of attack for Mach 6.0 and about 16 percent per degree for Mach 8.5. The magnitude and direction of lateral static pressure gradients change gradually with angle of attack and x/l station, as illustrated in figure 9. At angles of attack less than about 3° and stations at or upstream of x/l of about 0.719, positive lateral pressure gradients existed which would tend to drive the boundary layer towards the 0° radial plane. At all angles of attack for stations downstream of $x/l = 0.719$, the lateral pressure gradients would tend to drive the boundary layer towards the 90° radial plane.

Boundary-Layer Parameters

Theoretical boundary-layer computations have been performed by using the integro-differential boundary-layer method similar to that of reference 25 and described in appendix B. In these computations the transition from laminar to turbulent flow was initiated at the trip station, x/l value of 0.188. End of transition was computed to be

an x/l value of 0.312 for Mach 6.0 and 0.40 for Mach 8.5. The theoretical location for the end of transition for Mach 6.0 agreed reasonably well with oil flow data results.

Longitudinal distributions. - Results of the theoretical computations which are based on the experimental static pressure distributions are presented as longitudinal distributions for Mach 6.0 and 8.5 in figures 10(a) and 10(b), respectively. Zero angle-of-attack results were obtained in the three radial planes for both Mach numbers, and 5° angle-of-attack (windward side in $\phi = 0^\circ$ plane) results were obtained in the ϕ -planes of 0° and 90°. The experimental boundary-layer parameter distributions without trips are compared with theory at an x/l of 0.719 in the ϕ -plane of 0°. The values of the Mach 6.0 data at 0° angle of attack are somewhat greater than the corresponding theoretical values: greater by 10 percent for θ , 16 percent for δ^* , and 20 percent for δ . The installation of trips increased the experimental values of all three parameters by amounts on the order of 10 to 20 percent in the 0° ϕ -plane. A limited analytical study using the method of reference 25 indicated that the trip case could not be adequately modeled by simply increasing the local momentum thickness at the trip station by an amount equivalent to the trip drag because this effect dissipated completely with downstream distance. The theoretical estimates with trips are therefore not presented. Also, the method of reference 25 was modified to account for cross-flow effects. Calculations were performed for Mach 6.0 at 0° angle of attack and the results were within 1 percent of the results using the unmodified method and are therefore not shown. Data results with trips for 5° angle of attack are shown for Mach 6.0 in figure 10(a). Too few data measurements with no trips and $\alpha = 5^\circ$ were obtained within the boundary layer; thus no data results are shown. Observations of the data results of the three boundary-layer parameters and possible indications of cross flow are:

(1) For the data of 5° angle of attack with trips, the values for the 90° ϕ -plane are lower than for the 0° ϕ -plane for all three parameters. However, the trends of the 0° angle-of-attack theoretical predictions which do not account for cross flow are in the same direction; therefore, cross flow is not necessarily indicated.

(2) As the angle of attack is changed from 0° to 5°, values of the parameters generally decrease for both ϕ -planes of 0° and 90°; therefore, this result is inconclusive relative to cross flow.

(3) Figure 10(a) clearly shows for a comparison between $\phi = 0^\circ$ and 90° data with trips at $\alpha = 0^\circ$ that values of all three parameters are much less at $\phi = 90^\circ$ than at $\phi = 0^\circ$. The differences are larger than theory indicates, but theory did not account for cross flow. This result strongly suggests cross flow from $\phi = 90^\circ$ to $\phi = 0^\circ$ planes at $\alpha = 0^\circ$. In summary, these results indicate that only at $\alpha = 0^\circ$ is cross flow suggested from $\phi = 90^\circ$ to $\phi = 0^\circ$; the rest of the boundary-layer results are inconclusive.

At a Mach number of 8.5 only data obtained with trips at 0° angle of attack are shown because survey data for radial planes of 45° and 90° were in error.

Lateral distributions. - For Mach 6.0, the boundary-layer flow could be sufficiently analyzed to obtain experimental lateral distributions. The data results of the three boundary-layer parameters are, therefore, shown as a function of ϕ in figure 11. Trends shown, especially for $\alpha = 0^\circ$, are similar to trends that were expected for such a forebody design concept.

Flow-Field Surveys

Effect of swept compression. - Pitot pressure profiles within the boundary layer are presented in the top half of figure 12, and the inviscid flow profiles outside the boundary layer are presented in the bottom half of the figure. (All the experimental data are shown in the bottom portion.)

All measured pitot profiles in the boundary layer have higher values than those predicted by the method of reference 25 for all cases except for $M_\infty = 6.0$, $\alpha = 0^\circ$, and $\phi = 0^\circ$. Comparison of experimental and predicted velocity profiles (not included herein) showed reasonable agreement for Mach 6.0 and $\alpha = 0^\circ$ for all three planes. However, the indications were that the method for determining δ experimentally, discussed in appendix B, was not accurate enough for these cases. Smaller values of δ than those determined experimentally would have given better agreement. Furthermore, the velocity profile comparisons at $\alpha = 5^\circ$ and Mach 6.0 suggested that the trips may have affected the results noticeably at angle of attack. The Mach 8.5 data are believed to be affected by tube interference effects with the multitube pitot rake. Only the data in the $0^\circ \phi$ -plane appeared reasonably valid and are shown in the top portion of figure 12(c).

The Mach 6.0 and 8.5 inviscid flow measurements agree well with theory at 0° angle of attack. The effect on the Mach 6.0 inviscid flow field of increasing the angle of attack to 5° was slightly underpredicted for the $0^\circ \phi$ -plane, as shown in the bottom portion of figure 12(b). The $90^\circ \phi$ -plane theoretical pitot pressures are considerably lower than those predicted in the $0^\circ \phi$ -plane; however, the experimental data for the 5° angle-of-attack case are nearly identical at ϕ -planes of 0° and 90° ; this resulted in the $90^\circ \phi$ -plane values being greatly underpredicted.

Mach numbers at the edge of the boundary layer (M_δ) are noted in figures 12 to 15 for the inviscid flow-field profiles. These values correspond to the pitot and static pressures at the edge of the boundary layers and were determined during the analysis of the boundary-layer survey data.

Effects of axial station, boundary-layer trips, and angle of attack. - Pitot pressure profiles are presented in figure 13 for a series of axial stations for Mach 6.0. In the 0°

ϕ -plane the theory underpredicts the pitot pressure, particularly at the most downstream stations and at an angle of attack of 5° ; the underprediction was also evident in the 90° ϕ -plane at 5° angle of attack. These trends would be expected as a result of the irrotational flow assumption. The effects of boundary-layer trips on the flow-field pitot pressure distributions in the 0° ϕ -plane are shown by figure 14 to be negligible for an angle of attack of 0° and less than 5 percent at $\alpha = 5^\circ$. The theory predicts the no-trip cases well. Figures 15(a) and 15(b) show that increasing the angle of attack from 0° to 5° produces substantial increase (approximately 33 percent for $M_\infty = 6.0$ and approximately 51 percent for $M_\infty = 8.5$) in the pitot pressures in the 0° ϕ -plane at the x/l station of 0.719. However, when the body was rotated 90° so that the $\phi = 90^\circ$ plane was the windward side (fig. 15(b)), increasing the angle of attack to 5° had less effect (approximately 14-percent increase) at x/l of 0.719. This less effect resulted because more geometric compression has occurred in the 90° plane than in the 0° plane; thus the increased amount of compression because of the increased angle of attack is less significant (smaller percentage increase).

Cowl leading-edge flow field. - Mach numbers in the vicinity of the cowl leading edge are of interest in the design of an inlet. Lines of constant local Mach numbers are, therefore, shown in figure 16 for a free-stream Mach number of 6.0. The superimposed cowl leading edge of figure 16 was obtained by assuming that the leading edge in the ϕ -plane of 90° corresponded to the intersection of a conical bow shock of 7.5° half-angle cone at Mach 8.0 and the corresponding characteristic line emanating from the point of initial isentropic compression. The cowl leading edge in the ϕ -planes of 45° and 0° (physically no cowl) then corresponded to the intersection of the bow shock and a plane inclined 55° to the center line and passing through the cowl leading-edge point in the $\phi = 90^\circ$ plane (see model-design-concept section and fig. 1(a)). Axial locations of the cowl leading edge corresponding to the ϕ -planes of 0° , 45° , and 90° are x/l values of 0.931, 0.789, and 0.731, respectively.

Local Mach number values were obtained from the computational results using the computer program of references 7 and 8. Values used from the computer results were for axial positions which most nearly represented the cowl leading-edge positions; the x/l values were 0.907, 0.783, and 0.720 for the ϕ -planes of 0° , 45° , and 90° , respectively. Results for the 0° angle of attack in figure 16(a) indicate inconsistencies in the Mach number contour lines which are considered to be the result of the near constant wall slope of the centerbody surface in the ϕ -plane of 45° . In this area of inconsistencies, point values only are indicated in the 45° ϕ -plane. The contour lines are shown only in the inviscid flow field and the superimposed boundary-layer edge represents that determined experimentally with trips. About half of the inlet flow appears to be the boundary-layer flow.

At 5° angle of attack (windward side in the 0° ϕ -plane), the flow is compressed more in the 0° ϕ -plane than in the 45° and 90° ϕ -planes; this resulted in constant Mach number contour lines as depicted in figure 16(b). The boundary layer is somewhat thinner in the 0° ϕ -plane at 5° angle of attack; however, the amount of boundary layer occupying the inlet flow is only slightly less than that for 0° angle of attack. If the windward side were the 90° ϕ -plane, the boundary-layer thickness is expected to be thinner and thus the boundary layer would be a lesser amount of the total inlet flow.

It should be noted that for a full-scale vehicle the centerbody design radii would be reduced by an amount equal to the boundary-layer displacement thicknesses for the design conditions. Also, full-scale boundary-layer thicknesses should be much thinner relative to the centerbody radius and the cowl height because of the higher Reynolds numbers for the full-scale vehicle $\left(\frac{\text{Flight Reynolds number}}{\text{Tunnel Reynolds number}} \approx 50 \right)$.

Engine Cowl Location

The results show that at 0° angle of attack the boundary-layer parameters are smallest in the 90° ϕ -plane. The 5° angle-of-attack results are too inconclusive to determine if angle of attack with windward side in the $\phi = 0^\circ$ plane changes this trend. However, it is believed that if the ϕ -plane of 90° were the windward side, the boundary-layer parameters would become smaller. Since a small amount of angle of attack is expected during a normal cruise flight, the original design concept has been modified as shown in figure 17 to take better advantage of angle-of-attack flow conditions. The modifications are:

- (1) Rotate the forebody 90° so that the ϕ -plane of 90° is on the bottom of the vehicle.
- (2) Combine the cowls on the sides of the forebody into one cowl symmetric about the 90° ϕ -plane and extend the cowl so as to encompass the region from $\phi = 30^\circ$ to 150° .
- (3) Axially locate the cowl leading edge so that the leading compression characteristic intersects the cowl lip, point C in figure 17(b), at Mach 8.5 and "shock-on-lip" (point C) conditions exist at Mach 10.0.

With these modifications, positive lateral pressure gradients will exist over the entire angle-of-attack range of 0° to 5°. These lateral pressure gradients will tend to drive the boundary layer towards the 0° and 180° ϕ -planes or away from the relocated cowl entrance.

CONCLUSIONS

A preliminary analytical and experimental investigation has been conducted for a vehicle inlet forebody that was designed to have elliptical cross sections downstream of an initial sharp-nosed right circular cone. This concept resulted in the isentropic portion of the compression being performed in a swept manner. The investigations were conducted at Mach 6.0 and 8.5. Conclusions based on the results are as follows:

1. Near-characteristics and small-disturbance equation methods predict well the longitudinal pressure distribution of a nonaxisymmetric body such as the one tested in this investigation; both methods are very sensitive to the accuracy of surface contour inputs.
2. Inviscid flow-field conditions agree well at 0° angle of attack when predicted by the near method of characteristics, but become less accurate for increasing angle of attack.
3. Values of experimental no-trip boundary-layer thickness parameters were 10 to 20 percent greater than the results of the boundary-layer prediction method based on the experimental surface static pressures. The installation of trips increased the experimental thickness parameters on the order of 10 to 20 percent in the radial plane of 0° at 0° angle of attack; unsuccessful analytical attempts were made to model the trip effect by changing the momentum thickness at the trip station by an amount equivalent to the trip drag.
4. Lateral distributions of experimental static pressures and boundary-layer thickness parameters indicated that flow was directed from the major-axis plane (90° radial plane) to the minor-axis plane (0° radial plane) at 0° angle of attack; at 5° angle of attack with the windward side in the 0° radial plane, the results were, however, too inconclusive to ascertain a trend.
5. Improved forebody and inlet performance is expected if the inlet cowls on the sides of the forebody are combined into one cowl symmetric about the major-axis plane and relocated on the bottom of the forebody (windward side at positive angles of attack). Such a change would result in an increasing static pressure gradient with increasing angle of attack and, consequently, in the boundary-layer flow always being directed away from the inlet cowl entrance at zero and positive angles of attack.

Langley Research Center,
National Aeronautics and Space Administration,
Hampton, Va., December 23, 1974.

APPENDIX A

INVISCID FLOW-FIELD THEORIES

The inviscid external flow field was analyzed with the help of two different three-dimensional flow-field analysis programs; comparisons were made of the accuracy, speed, and ease of computation. The first method is referred to as the method of near characteristics while the second method uses unified supersonic/hypersonic small-disturbance equations.

Method of Near Characteristics

The method of near characteristics, which was developed for inviscid perfect gas flow fields, is described in reference 7 and the user's manual is reference 8. Calculations proceed downstream in selected reference planes employing a network of near characteristics resulting from the intersection of characteristic surfaces with the planes. The program was developed for relatively slender smooth-surfaced bodies operating at moderately supersonic Mach numbers; therefore, irrotational flow was assumed, i.e., the entropy behind the shock waves is assumed to be constant. Rotational flow would be produced by blunted bodies, especially at hypersonic speeds, or bodies at high angles of attack. Compatibility relations, which prescribe the variation of the local velocity components along the near characteristics, are derived in circular cylindrical coordinates. The solutions in each of the reference planes are coupled through terms, appearing in the compatibility relations, that involve transverse derivatives. The derivatives are determined by spline fitting without special interpolation of the values of the velocity components.

In reference 7 results of this method were compared with limited experimental data, which sometimes resulted in slight differences. These differences were generally attributable to entropy variations or viscous effects. Also, embedded shocks were found to arise in the flow fields around an axisymmetric body at angle of attack and around nonaxisymmetric compression surfaces. When the starting solution is nonaxisymmetric (e.g., a cone at angle of attack), care must be taken to ensure that the velocity components, together with the transverse derivatives resulting from their curve fit, satisfy the body boundary conditions. If these conditions are not satisfied, artificial pressure waves are introduced, propagating outward from the body surface.

Initial flow-field data must be provided to start the numerical solution; the program was initially envisioned for sharp-nosed circular and elliptic cones. In each meridian plane at a given x-location an equal number of mesh points is evenly spaced along a radial line between the body and the associated shock; the conditions at each point are

APPENDIX A - Continued

obtained from cone tables (e.g., ref. 26) or cone solutions from computer programs. If the body is at small angles of attack, tables similar to reference 27 can be used or the conditions can be obtained by calculating asymptotic solutions with the present numerical method. This is done by using the initial conditions obtained for a right circular cone at zero angle of attack and then performing the calculations for the right circular cone at angle of attack for a sufficient body length to allow the conditions in all meridian planes to asymptotically approach steady conditions. For the body of this present investigation, the conditions for Mach 6.0 and an angle of attack of 5° had to be obtained in increments; that is, initial conditions for zero angle of attack were used for computations at 1° angle of attack. The conditions obtained from the 1° angle-of-attack computations were then used for initial conditions for 2° angle-of-attack computations; this procedure was continued up to an angle of attack of 5° .

The program as described in references 7 and 8 incorporates spline fits for the body points which are input as x and y coordinates in various meridional planes. In the present investigation the computer program with the original spline fit intact was used, but the resulting surface static pressure distributions oscillated and disagreed with experimental pressure distributions. Such oscillations can be alleviated by using various methods, such as defining the body more smoothly by incorporating least-square fits for the body coordinate inputs or defining as input the point slopes corresponding to the coordinate inputs. The method chosen introduced into the computer program (refs. 7 and 8) an option that allowed the incorporation of point slope values as input.

The surface contour of the body was corrected for the boundary-layer displacement thickness, which was obtained in an iterative manner by using the present near-characteristics-method computer program and the boundary-layer program described in reference 25 and modified as described in appendix B.

Numerical Solution to Three-Dimensional Unified Supersonic/Hypersonic Small-Disturbance Equations

The numerical solution to three-dimensional unified supersonic/hypersonic small-disturbance equations is described in references 23 and 24; this method provides a numerical solution to the nonlinear disturbance equations embodied in the unified supersonic/hypersonic theory developed by Van Dyke. The small-disturbance equations are applicable for both supersonic and hypersonic flow over configurations whose local surface inclinations to the free stream are small. The numerical method uses the Lax-Wendroff finite-difference approximation to the flow equations for updating the flow field in a cross-cut plane. Special treatment is required of points on or near the boundary contour: (1) boundary points are updated by using either a quasi-one-dimensional method of characteristics (used in the present investigation) or a conservative difference

APPENDIX A - Concluded

scheme derived from the Lax-Wendroff difference equations and (2) field points near the boundary contour are updated by interpolation. This method allows determination of the complete flow field in addition to the surface properties. Shock waves and other discontinuities are accounted for implicitly in the numerical method.

The initial conditions are generated for this program by using one of three options: (1) initial conditions are computed from cone tables, (2) initial conditions are computed by using the tangent wedge method, or (3) initial conditions are set to free-stream conditions and an "impulsive start" method is employed. For this investigation the cone-table method was used.

Surface contours were input by a pointwise definition of the axial variation of the semimajor and semiminor axis of elliptical cross sections. The program then connects the points by a linear cubic spline with specified slope discontinuities. The contours were physical model measurements and were not corrected for boundary-layer displacement thicknesses.

APPENDIX B

VISCOUS FLOW FIELD

Theory

During this investigation the boundary-layer thickness parameters were predicted using an integrodifferential boundary-layer method. The basic integral method used is applicable to the prediction of axisymmetric and two-dimensional turbulent boundary layers and is similar to that of reference 25. The method employs the simultaneous solution of the integral-momentum, moment-of-momentum, and energy equations. Non-equilibrium boundary-layer velocity profiles can be computed by using this method which employs the modified Crocco relation for the enthalpy velocity profile relation of reference 28. The present version of the boundary-layer prediction method is somewhat more complex than that of reference 25 in that provisions for real gas and nonisentropic boundary-layer edge conditions are included. Several simplifying assumptions are retained, such as a flat-plate shear stream profile and no provisions being incorporated for a normal pressure gradient. Revisions were made to the computer program for the present investigation to account for the effects of boundary-layer trips and small amounts of cross flow in the plane of symmetry. Trip effects were accounted for by estimating the drag of the trips and then increasing the initial momentum thickness θ by that amount. This approach was used with the realization that this method of accounting for the trips is somewhat inadequate; however, the computer program used was readily modified for such a method. The cross-flow effect was accomplished by incorporating into the computer program the proper cross-flow terms.

During the present investigation, this method was employed for ideal-gas computations in the various meridian planes; each plane was treated as an axisymmetric body contour. Distributions of static pressure, boundary-layer-edge Mach number, and wall temperature are required program input. The static pressure distributions employed were those obtained experimentally and extrapolated to the model nose. Mach number distributions were obtained from the results of the near-characteristics computer program. Temperatures were not measured; therefore, the wall-temperature distributions were assumed to be adiabatic. This temperature assumption applies closely for the Mach 6.0 case because the wind tunnel was preheated prior to the test and the test times were relatively long. However, at Mach 8.5 conditions, the tunnel was not preheated and the test times were much shorter.

Experimental Boundary-Layer Thickness Parameters

The program was used to predict at given longitudinal stations the conditions across the boundary layer and the various boundary-layer parameters such as velocity thickness

APPENDIX B – Concluded

δ , displacement thickness δ^* , and momentum thickness θ . Comparisons of the analytical and experimental pitot pressure profiles were performed directly. However, two additional assumptions were required in order to obtain experimental boundary-layer thickness parameters. First, the edge of the velocity thickness δ was assumed to correspond to the peak values in the profiles of pitot pressures measured within the body flow field. These profiles typically showed a slow increase in pitot pressure followed by a rapid decrease in pitot pressure as the wall was approached. Second, a constant value of static pressure was assumed to exist across the boundary layer and to be equal to the measured wall static pressure. An attempt was made to verify these assumptions by determining a static pressure profile across the body flow field. Since static pressure was not measured in the flow, values for this profile were obtained by first calculating the ratio of local static to pitot pressure with the inviscid-flow computer program of reference 8. These calculated local ratio values were then multiplied by the corresponding measured local-pitot pressures. As would be expected, the static pressure profiles near the wall were the same as those exhibited by the pitot pressure profiles. The peak point of the two types of profiles were similarly located in height off the model wall (δ). Also, more importantly, the peak point static pressure value was nearly equal to the wall static pressure value measured at Mach 6.0 and 0° angle of attack. This agreement of the static pressures indicates that the assumptions of the location of the boundary-layer edge at the peak point in the pitot pressure profile and of constant static pressure across the boundary layer were generally reasonable. However, the assumption of constant static pressure was found to be invalid at Mach 6.0 in the ϕ -plane of 45° at 0° angle of attack and in the ϕ -planes of 0° and 90° at 5° angle of attack. In these cases the measured wall static pressure value was slightly greater than all values in the static pressure profile; therefore, in such cases a profile with slightly increasing static pressure values from the boundary-layer edge (peak-point value) to the wall (measured value) was assumed. The assumed static pressures and the measured pitot pressures were used to determine the Mach number and temperature distributions across the boundary layer, which then were used in equations (B1) and (B2) in integrations to obtain the experimental displacement thickness δ^* and the momentum thickness θ , respectively.

$$\delta^* = \int_0^\delta \left[1 - \frac{\rho u}{(\rho u)_\delta} \right] dy = \int_0^\delta \left(1 - \frac{M/M_\delta}{\sqrt{T/T_\delta}} \right) dy \quad (B1)$$

$$\theta = \int_0^\delta \left[\frac{\rho u}{(\rho u)_\delta} \left(1 - \frac{u}{u_\delta} \right) \right] dy = \int_0^\delta \left[\frac{M/M_\delta}{\sqrt{T/T_\delta}} - \left(\frac{M}{M_\delta} \right)^2 \right] dy \quad (B2)$$

APPENDIX C

SCHLIEREN PHOTOGRAPHS

Some representative schlieren photographs obtained during the Mach 6.0 and 8.5 experimental investigation are included in figure 18. Enlargements of these photographs were used to obtain the experimental measurements included in figure 5. The survey probe is in view in the photographs, but the measurements were obtained upstream of the probe or in the region not affected by the presence of the probe.

Disturbances due to the presence of boundary-layer trips are not detectable at Mach 6.0 but are detectable at Mach 8.5 as seen in figures 18(c) and 18(d), respectively.

APPENDIX D

OIL-STREAK TEST RESULTS

Oil-streak tests were conducted at Mach 6.0 for 0° and 5° angles of attack with and without boundary-layer trips installed. Photographic results of these tests are presented in figures 19 and 20 for α of 0° and 5° , respectively. At least one row (one radial plane) of surface static pressure orifices is visible in each photograph for use as a reference line. In order for a row of orifices to be visible in figure 20, the viewing direction was not perpendicular to the windward side plane (see insert sketch) as was the case for the photographs in figure 19. The oil-streak tests at $\alpha = 5^\circ$ were performed with the ϕ -plane of 180° , the windward side. Since the model was symmetric, however, the results were the same as if the ϕ -plane of 0° were the windward side; this was the case when the surface-static-pressure data and pitot-survey data were obtained.

A slight amount of cross flow toward the $0^\circ \phi$ -plane exists for 0° angle of attack and is more detectable in the photograph for the no boundary-layer trip case, figure 19(b). With only one row of orifices visible for a reference line in the photographs for 5° angle-of-attack (fig. 20) cases, the existence of cross flow away from the $180^\circ \phi$ -plane (windward-side plane) is somewhat difficult to ascertain; however, from observations at the time the photographs were taken, cross flow away from the windward-side plane did appear to exist.

In order to better understand the streamline patterns for angle of attack, a computer program (ref. 10) that traces streamlines through a three-dimensional flow field was written in conjunction with the computer program of references 7 and 8. The calculated surface inviscid streamline patterns for a Mach number of 6.0 and 3° angle of attack are shown in a planform view in figure 21. Body streamlines, the solid lines of figure 21, are shown for reference purposes. Departure of the streamlines from their respective radial planes is significant and increases with increasing axial station. Streamlines for a viscous layer would be expected to depart even further from the body reference streamlines than do the inviscid flow streamlines shown; this is expected since the fluid in the viscous layer has a lower momentum than the inviscid flow and is subject to the same lateral pressure gradient.

REFERENCES

1. Becker, John V.: New Approaches to Hypersonic Aircraft. Paper presented at the Seventh Congress of the International Council of the Aeronautical Sciences (Rome, Italy), Sept. 1970.
2. Becker, John V.: Prospects for Actively Cooled Hypersonic Transports. *Astronaut. & Aeronaut.*, vol. 9, no. 8, Aug. 1971, pp. 32-39.
3. Henry, John R.; and Beach, H. Lee: Hypersonic Air-Breathing Propulsion Systems. *Vehicle Technology for Civil Aviation - The Seventies and Beyond*, NASA SP-292, 1971, pp. 157-177.
4. Becker, John V.; and Kirkham, Frank S.: Hypersonic Transports. *Vehicle Technology for Civil Aviation - The Seventies and Beyond*, NASA SP-292, 1971, pp. 429-445.
5. Henry, John R.; and Anderson, Griffin Y.: Design Considerations for the Airframe-Integrated Scramjet. NASA TM X-2895, 1973.
6. Anderson, Griffin Y.; Agnone, Anthony M.; and Russin, Wm. Roger: Composition Distribution and Equivalent Body Shape for a Reacting, Coaxial, Supersonic Hydrogen-Air Flow. NASA TN D-6123, 1971.
7. Scheuing, Richard Albert: Three Dimensional Supersonic Flow Over a Smooth Body With Shock-Producing Protuberance. Ph. D. Thesis, Univ. of New York, 1971.
8. Lehrhaupt, Harry: Supersonic Flow Calculations for a Cone With an Elliptic Flare. NASA CR-112301, 1970.
9. Miyazawa, M.: A New Technique for Inducing a Turbulent Boundary Layer in a Supersonic Flow. *Proceedings of the 10th International Symposium on Space Technology and Science*, AGNE Pub., Inc., 1973, pp. 451-459.
10. Agnone, Anthony M.; and Kung, Fanny: Computer Program for Assessing the Theoretical Performance of a Three-Dimensional Inlet. NASA CR-112304, 1973.
11. Agnone, Anthony Michael: Design and Theoretical Performance Estimate of a Three Dimensional Integrated Scramjet Engine. Ph. D. Thesis, Univ. of New York, 1973.
12. Piva, Renzo: Leading Edge Cooling by Upstream Injection. NASA CR-111965, 1973.
13. Piva, Renzo: Interaction Between an Upstream Facing Wall Jet and a Supersonic Stream. *AIAA J.*, vol. 11, no. 1, Jan. 1973, pp. 6-7.
14. Agnone, Anthony M.: Slipstream Formed by a Supersonic Source in a Hypersonic Stream. *AIAA J.*, vol. 9, no. 7, July 1971, pp. 1419-1421.

15. Agnone, Anthony: Cross-Flow Effects on the Boundary Layer in a Plane of Symmetry. *J. Spacecraft & Rockets*, vol. 11, no. 7, July 1974, pp. 542-544.
16. Saland, Heywood; Fox, Herbert; and Hoydysh, Walter: Studies of Engine-Airframe Integrated Hypersonic Vehicles. NASA CR-112300, 1973.
17. Agnone, Anthony M.: Scramjet Fuel Injector Design Parameters and Considerations - Development of a Two-Dimensional Tangential Fuel Injector With Constant Pressure at the Flame. NASA CR-112302, 1972.
18. Cavalleri, R. J.; and Agnone, A. M.: Description of a Computer Program To Calculate Reacting Supersonic Internal Flow Fields With Shock Waves Using Viscous Characteristics - Program Manual and Sample Calculations. NASA CR-112303, 1973.
19. Schaefer, William T., Jr.: Characteristics of Major Active Wind Tunnels at the Langley Research Center. NASA TM X-1130, 1965.
20. Goldberg, Theodore J.; and Hefner, Jerry N. (With appendix by James C. Emery): Starting Phenomena for Hypersonic Inlets With Thick Turbulent Boundary Layers at Mach 6. NASA TN D-6280, 1971.
21. Ferri, Antonio; and Fox, Herbert: Analysis of Fluid Dynamics of Supersonic Combustion Process Controlled by Mixing. Twelfth Symposium (International) on Combustion, Combustion Inst., 1969, pp. 1105-1113.
22. Henry, J. R.; and McLellan, C. H.: Air-Breathing Launch Vehicle for Earth-Orbit Shuttle - New Technology and Development Approach. *J. Aircraft*, vol. 8, no. 5, May 1971, pp. 381-387.
23. Gunness, R. C., Jr.; Knight, C. J.; and D'Sylva, E.: Flow Field Analysis of Aircraft Configurations Using a Numerical Solution to the Three-Dimensional Unified Supersonic/Hypersonic Small-Disturbance Equations. Part I. NASA CR-1926, 1972.
24. D'Sylva, E.: Flow Field Analysis of Aircraft Configurations Using a Numerical Solution to the Three-Dimensional Unified Supersonic/Hypersonic Small-Disturbance Equations. Pt. II. NASA CR-1927, 1972.
25. Pinckney, S. Z.: Method for Predicting Compressible Turbulent Boundary Layers in Adverse Pressure Gradients. NASA TM X-2302, 1971.
26. Sims, Joseph L.: Tables for Supersonic Flow Around Right Circular Cones at Zero Angle of Attack. NASA SP-3004, 1964.
27. Sims, Joseph L.: Tables for Supersonic Flow Around Right Circular Cones at Small Angle of Attack. NASA SP-3007, 1964.

28. Pinckney, S. Z.: Static-Temperature Distribution in a Flat-Plate Compressible Turbulent Boundary Layer With Heat Transfer. NASA TN D-4611, 1968.

REPRODUCIBILITY OF THE
ORIGINAL PAGE IS POOR

26

TABLE 1. - TEST CONDITIONS

M_∞	α , deg	Windward-side ϕ -plane, deg	$P_{t,\infty}$, atm	$T_{t,\infty}$, K	R per meter	Boundary-layer trips at $x/l = 0.188$	Static pressure distribution	Pitot survey		Survey-rake shaft angle, ϵ , deg (a)	Oil streaks
								x/l station	ϕ -plane, deg		
6.0	0 to 5	0	12.245 19.050 25.510	505.56	0.984×10^7 1.476 1.969	Yes	Yes	----	---	---	---
		0	12.245 19.050	505.56	.984 1.476	Yes	Yes	0.719 .750 .789 .931	0	---	---
	0	---	19.050	505.56	1.476	Yes	Yes	.719 .750 .789	45	---	---
	0 and 5	0	19.050	505.56	1.476	Yes	Yes	.719 .731	90	---	---
	0 and 5	0	19.050	505.56	1.476	No	Yes	.719	0	---	---
	0 to 5	0	12.245 19.050	505.56	.984 1.476	No	Yes	----	---	---	---
	0 and 5	0	19.050	505.56	1.476	Yes No	---	----	---	---	Yes
	0 to 5	0	102.04	838.89	1.476×10^7	Yes	Yes	----	---	---	---
	0 and 2	0	102.04	838.89	1.476	No	Yes	----	---	---	---
	0 and 5	0	102.04	838.89	1.476	Yes	Yes ^c	0.719	0	10	---
8.5	0	---	102.04	838.89	1.476	Yes	Yes ^c	.719	45	17	---
	0 and 5	90	102.04	838.89	1.476	Yes	Yes ^c	.719	90	17	---
	0	---	102.04	838.89	1.476	No	No	.375	90	17	---
	0 and 5	0	102.04	838.89	1.476	No	Yes ^c	.719	0	8 10	---

^aSee figure 4(b).

^bAngle of attack in 1° increments.

^cLimited static pressure measurements.

TABLE 2.- COORDINATE EQUATIONS FOR ORIGINAL DESIGN CONCEPT

(a) $\phi = 0^\circ$ (minor-axis plane).

$$\begin{cases} 0 \leq x \leq 0.58125 \\ r = 0.13165x \end{cases}$$

$$\begin{cases} 0.58125 \leq x \leq 0.64776 \\ r = 0.26157x^2 - 0.17039x + 0.08722 \end{cases}$$

$$\begin{cases} 0.64776 \leq x \leq 0.72515 \\ r = 0.25723x^2 - 0.16383x + 0.08485 \end{cases}$$

$$\begin{cases} 0.72515 \leq x \leq 0.80044 \\ r = 0.23978x^2 - 0.13803x + 0.07533 \end{cases}$$

$$\begin{cases} 0.80044 \leq x \leq 0.85643 \\ r = 0.01519x^2 + 0.22311x - 0.06972 \end{cases}$$

$$\begin{cases} x \geq 0.85643; A = 0.85643; B = x - A \\ r = 0.13254 + 0.27416B + 0.05488B^2 - 0.60181B^3 + 20.57292B^4 \end{cases}$$

(b) $\phi = 90^\circ$ (major-axis plane).

$$\begin{cases} 0 \leq x \leq 0.38061 \text{ (Designed end of cone, 15.468 cm)} \\ r = 0.13165x \end{cases}$$

$$\begin{cases} 0.38061 \leq x \leq 0.44713 \\ r = 0.26157x^2 - 0.06545x + 0.03714 \end{cases}$$

$$\begin{cases} 0.44713 \leq x \leq 0.52451 \\ r = 0.25722x^2 - 0.06062x + 0.03591 \end{cases}$$

$$\begin{cases} 0.52451 \leq x \leq 0.59981 \\ r = 0.23978x^2 - 0.04182x + 0.03086 \end{cases}$$

$$\begin{cases} 0.59981 \leq x \leq 0.65571 \\ r = 0.01519x^2 + 0.22921x - 0.05076 \end{cases}$$

$$\begin{cases} x \geq 0.65571; A = 0.65571; B = x - A \\ r = 0.10612 + 0.27416B + 0.05488B^2 - 0.60181B^3 + 20.57292B^4 \end{cases}$$

TABLE 3.- MEASURED MODEL COORDINATES

x/l	r/l at -								
	$\phi = 0^\circ$	$\phi = 22.5^\circ$	$\phi = 45^\circ$	$\phi = 67.5^\circ$	$\phi = 90^\circ$	$\phi = 270^\circ$	$\phi = 292.5^\circ$	$\phi = 315^\circ$	$\phi = 337.5^\circ$
0.0625	0.0076	0.0077	0.0079	0.0081	0.0084	0.0082	0.0081	0.0078	0.0078
.1250	.0152	.0152	.0156	.0160	.0164	.0156	.0154	.0152	.0154
.1875	.0236	.0237	.0242	.0246	.0250	.0238	.0236	.0236	.0237
.2500	.0318	.0320	.0326	.0329	.0333	.0320	.0318	.0317	.0318
.3125	.0400	.0402	.0408	.0411	.0415	.0399	.0398	.0398	.0399
.3750	.0479	.0481	.0491	.0493	.0500	.0483	.0481	.0479	.0480
.4219	.0542	.0544	.0559	.0564	.0573	.0556	.0555	.0550	.0548
.4531	.0586	.0590	.0607	.0616	.0627	.0608	.0607	.0599	.0592
.4844	.0648	.0634	.0657	.0672	.0684	.0662	.0662	.0652	.0638
.5156	.0669	.0679	.0710	.0732	.0745	.0726	.0722	.0706	.0683
.5469	.0711	.0726	.0766	.0798	.0811	.0796	.0789	.0762	.0729
.5781	.0756	.0777	.0826	.0868	.0882	.0871	.0859	.0819	.0778
.6094	.0808	.0831	.0890	.0941	.0958	.0949	.0932	.0879	.0831
.6406	.0865	.0891	.0958	.1019	.1036	.1030	.1011	.0948	.0891
.6719	.0926	.0954	.1028	.1099	.1119	.1114	.1093	.1021	.0954
.7031	.0989	.1019	.1099	.1181	.1207	.1203	.1176	.1095	.1021
.7375	.1061	.1093	.1181	.1272	.1305	.1303	.1268	.1176	.1096
.7656	.1123	.1156	.1249	.1346	.1382	.1381	.1340	.1241	.1161
.7969	.1195	.1231	.1325	.1424	.1462	.1459	.1414	.1316	.1234
.8281	.1274	.1311	.1402	.1498	.1532	.1528	.1482	.1390	.1312
.8594	.1363	.1395	.1479	.1567	.1594	.1589	.1546	.1464	.1395
.8906	.1457	.1482	.1553	.1632	.1645	.1635	.1602	.1536	.1479
.9219	.1544	.1563	.1617	.1678	.1684	.1676	.1649	.1601	.1564
.9375	.1584	.1599	.1644	.1693	.1700	.1694	.1668	.1630	.1602
.9685	.1655	.1666	.1686	.1717	.1727	.1724	.1699	.1674	.1664
.9925	.1680	.1693	.1695	.1728	.1744	.1736	.1720	.1688	.1684

TABLE 4.- STATIC PRESSURE ORIFICE LOCATIONS

x/l	$\phi = 0^\circ$			$\phi = 45^\circ$			$\phi = 90^\circ$		
	$M_\infty = 6.0$	$M_\infty = 8.5$		$M_\infty = 6.0$	$M_\infty = 8.5$		$M_\infty = 6.0$	$M_\infty = 8.5$	
		During statics	During surveys		During statics	During surveys		During statics	During surveys
0.4375				✓			✓		
.5000	✓	✓	✓	✓	✓	✓	✓	✓	
.5625	✓			✓			✓		
.6250	✓	✓	✓	✓	✓	✓	✓	✓	
.6565	✓			✓			✓		
^a .6880	✓	✓	✓	✓	✓	✓	✓	✓	
^b .7185	✓	✓	✓	✓	✓	✓	✓	✓	
.7315							✓	✓	
.7500	✓	✓	✓	✓			✓	✓	
.7893	✓	✓	✓	✓	✓	✓	✓		
.8125	✓	✓	✓	✓			✓		
.8440	✓	✓	✓	✓	✓	✓			
.8750	✓	✓	✓						
.9065	✓	✓	✓						
.9315	✓								

^aOrifices also located in meridian planes of 270° and 315° at Mach 6.0 and 270° at Mach 8.5.

^bOrifices also located in meridian planes of 0° , 8° , 12° , and 16° at Mach 8.5.

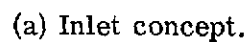
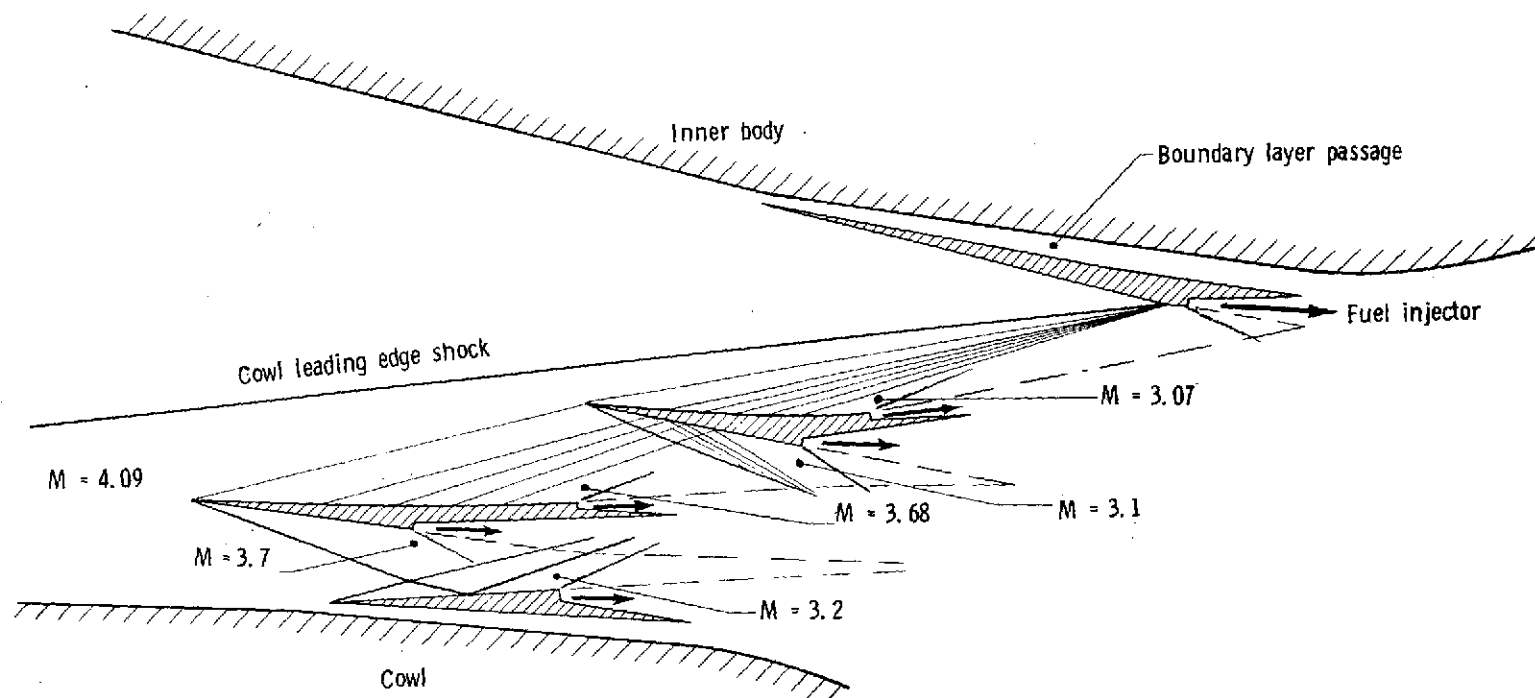
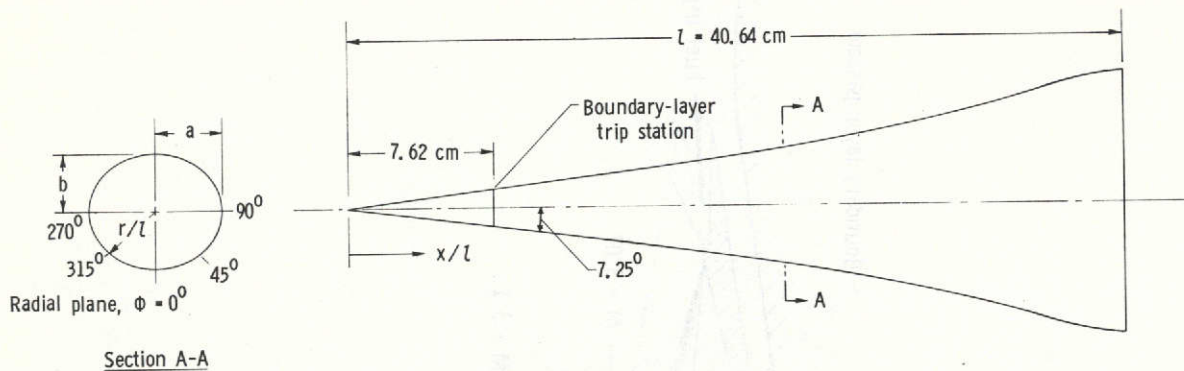


Figure 1.- Schematic of NASA-NYU design concept.

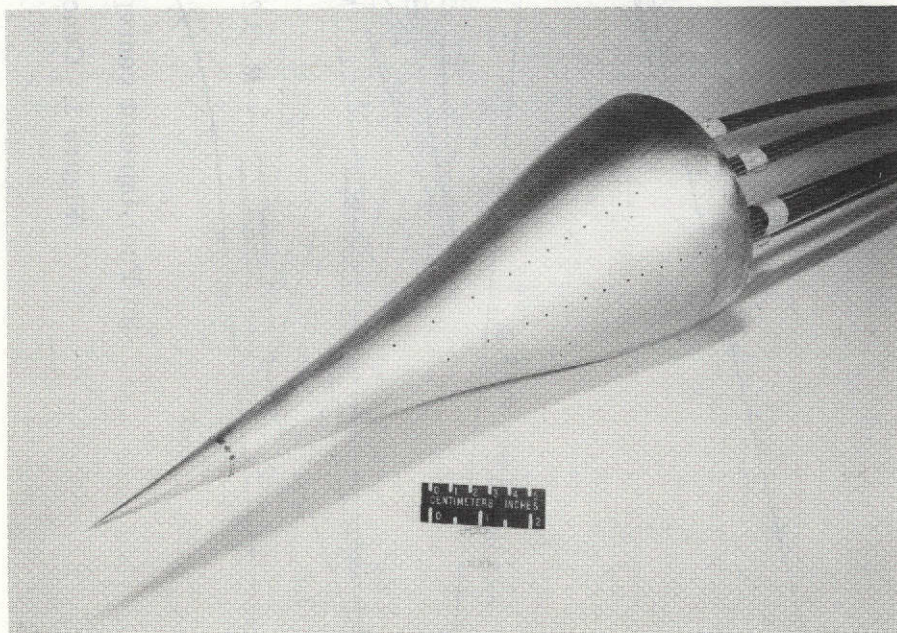


(b) Fuel-injector concept; $M_\infty = 6.0$.

Figure 1.- Concluded.



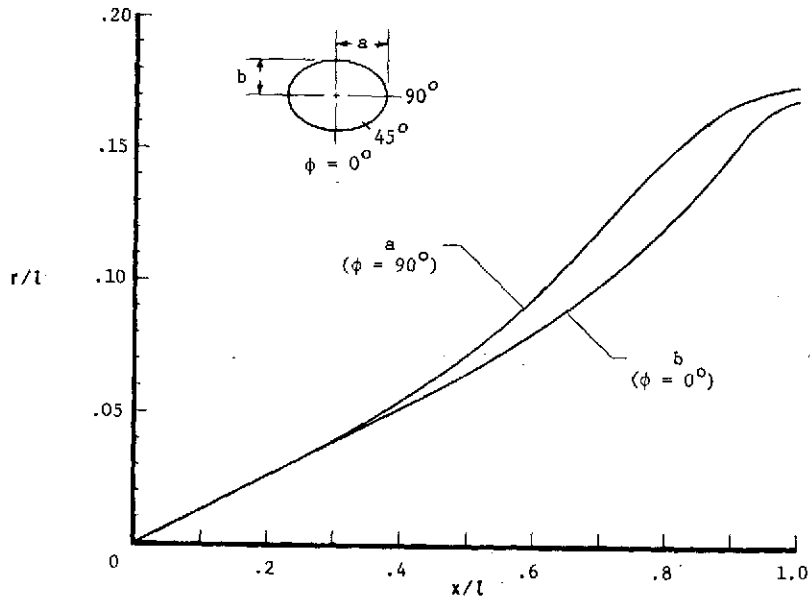
(a) Model schematic.



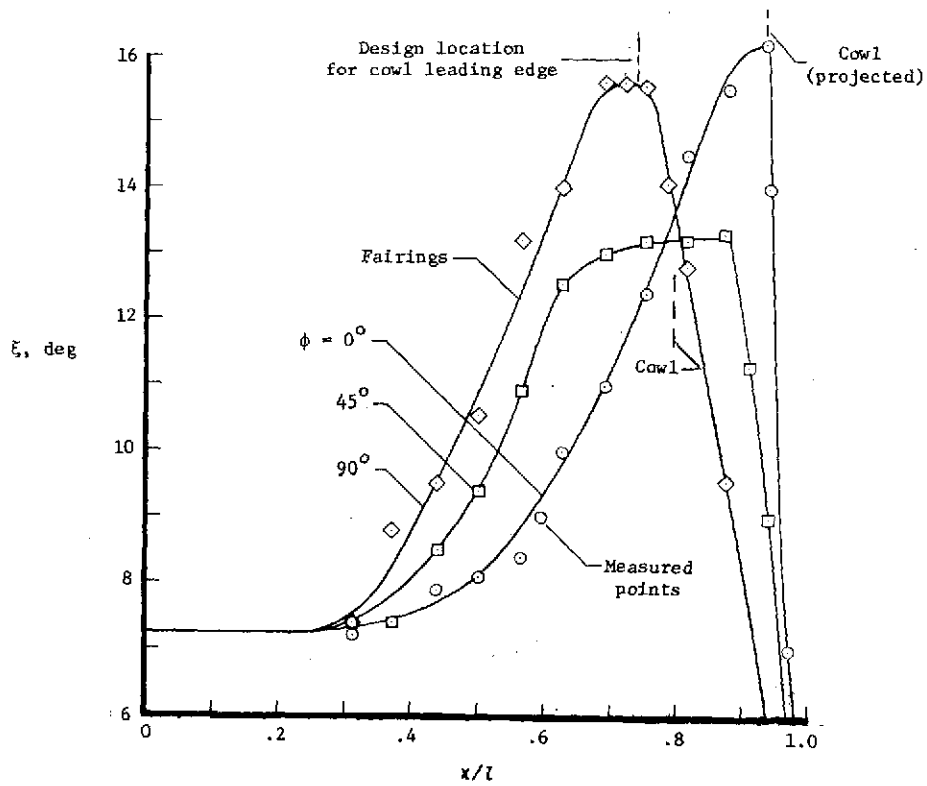
L-75-122

(b) Model photograph.

Figure 2.- Nonaxisymmetric inlet centerbody.

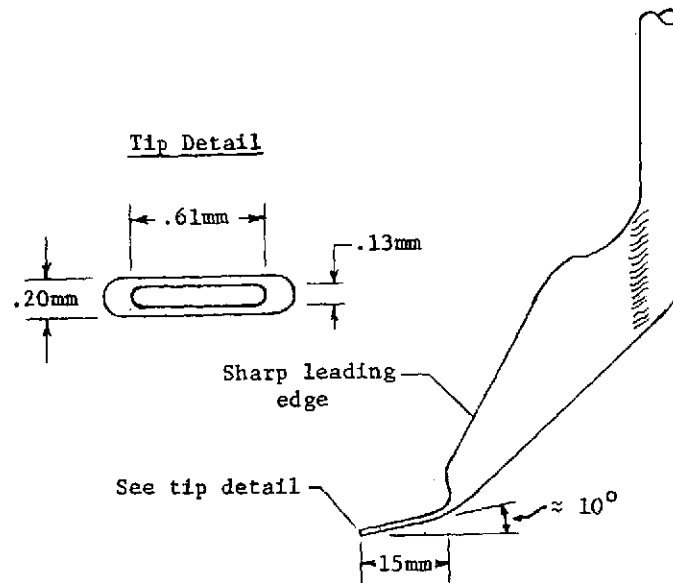


(a) Measured coordinates for major and minor axes.



(b) Surface angle in three radial planes.

Figure 3.- Physical parameters of fabricated model.

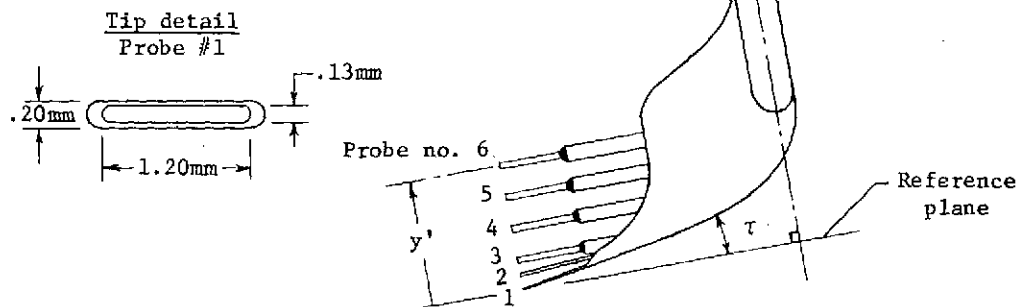


(a) Single probe; $M_\infty = 6.0$.

Probe	y', cm	Probe I.D., cm	Probe O.D., cm	τ, deg
1	.010	see sketch	see sketch	10
2	.254	.0254	.0508	5
3	.508	.0508	.1016	0
4	1.016			
5	1.524			
6	2.302			

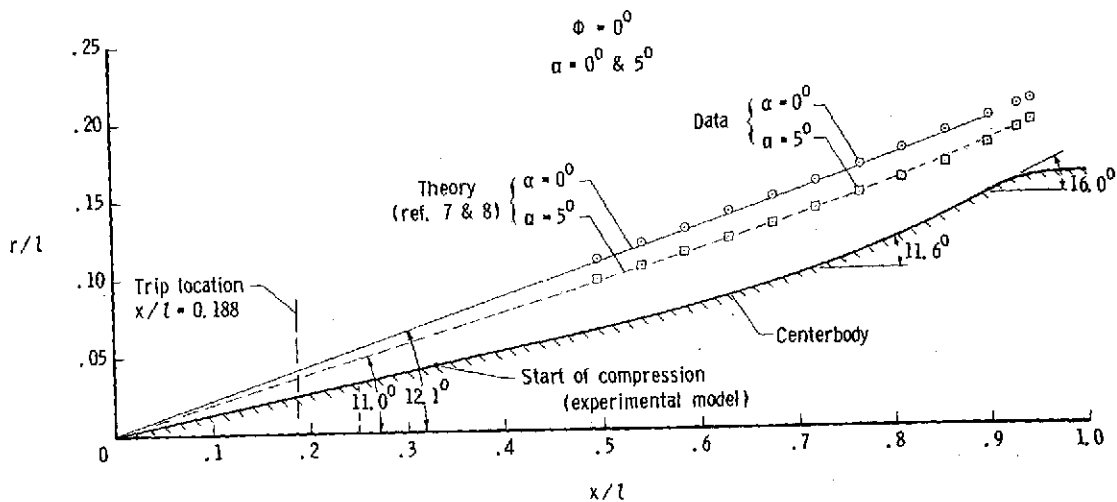
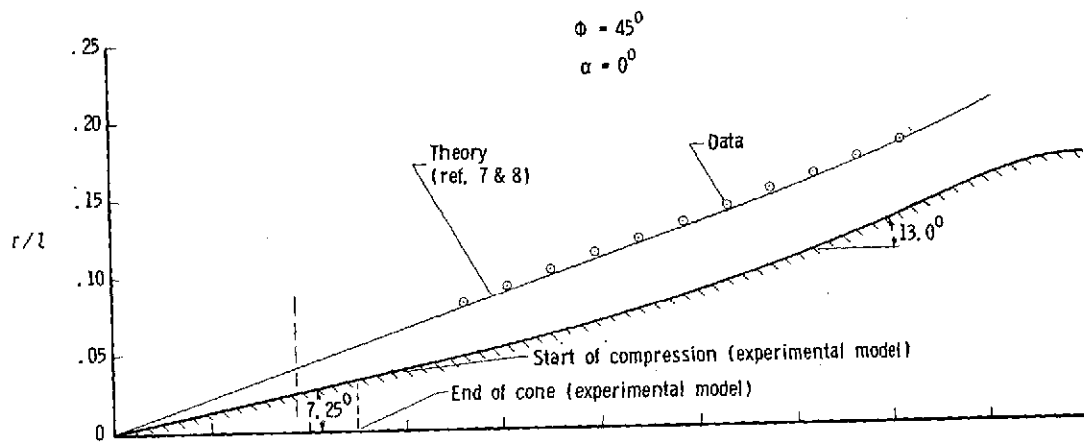
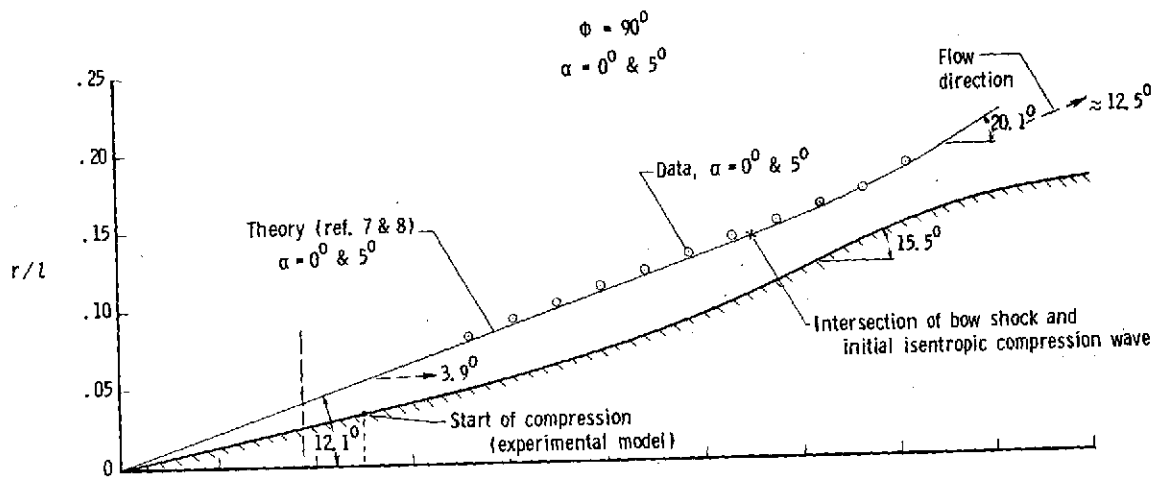
Note: 1) See table 1 for ϵ values.

2) Each probe was connected in parallel to a $0-1.31 \times 10^5 \text{ N/m}^2$ baratron and a $0-3.45 \times 10^5 \text{ N/m}^2$ pressure transducer.



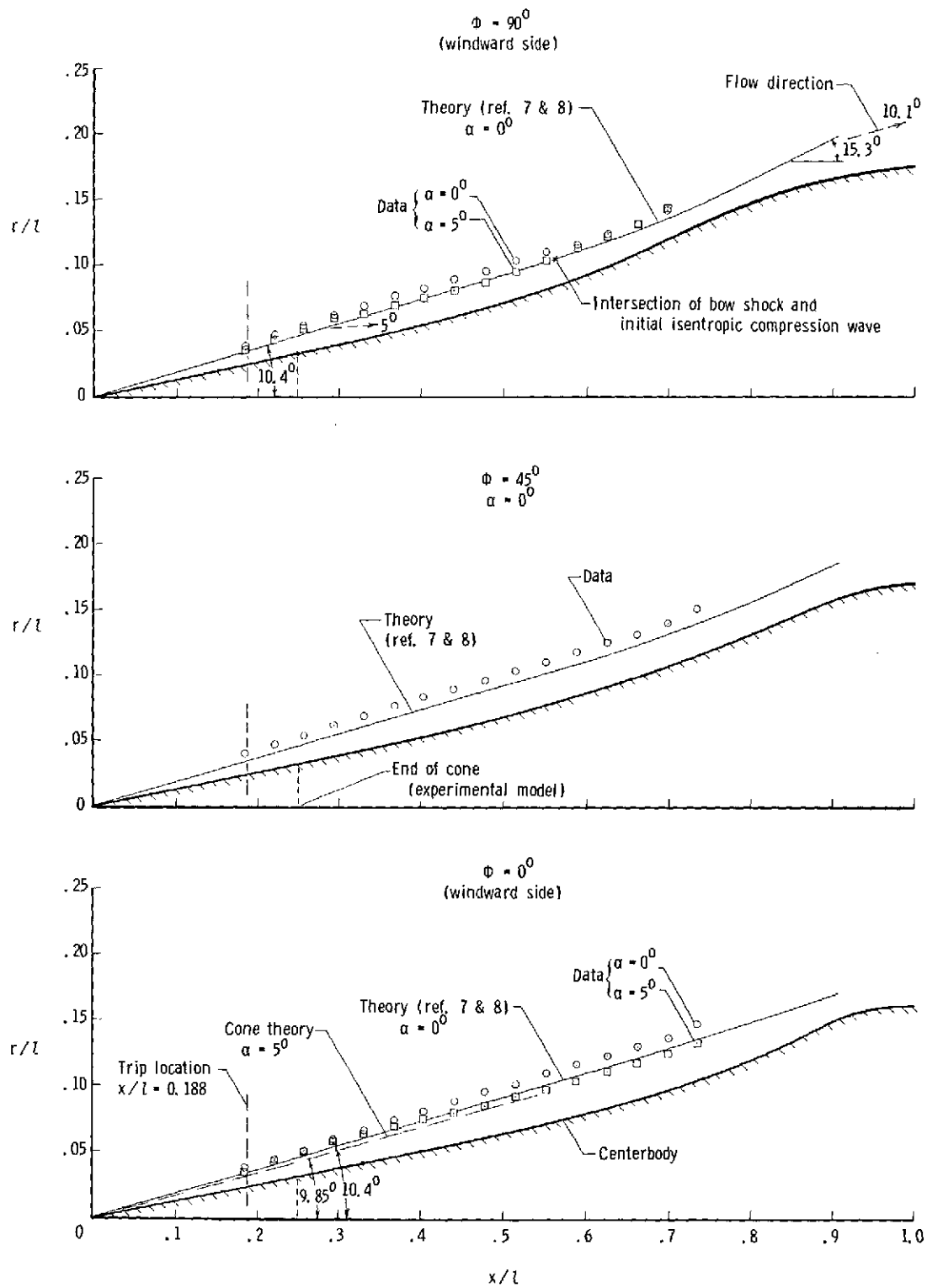
(b) Multiple probe survey rake; $M_\infty = 8.5$.

Figure 4.- Schematic of pitot-pressure survey rakes.



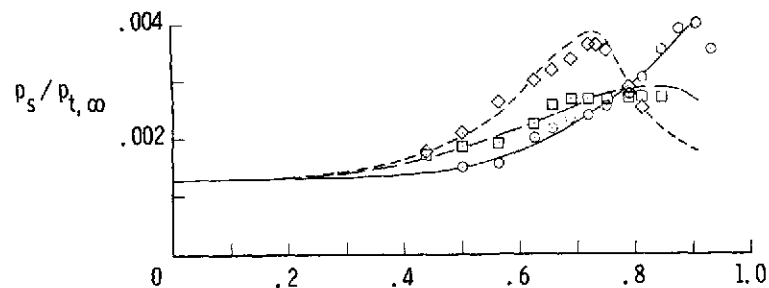
(a) $M_\infty = 6.0$; $\phi = 0^\circ$ (windward side).

Figure 5.- Typical experimental and theoretical shock correlations.

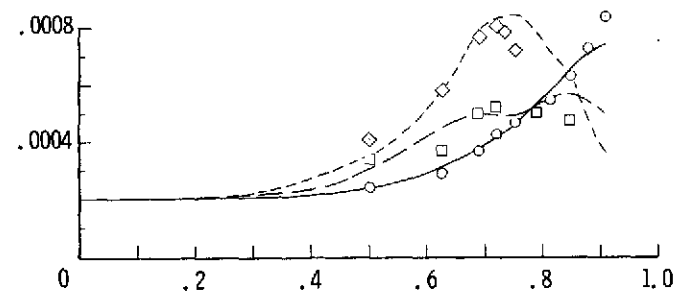


(b) $M_\infty = 8.5$.

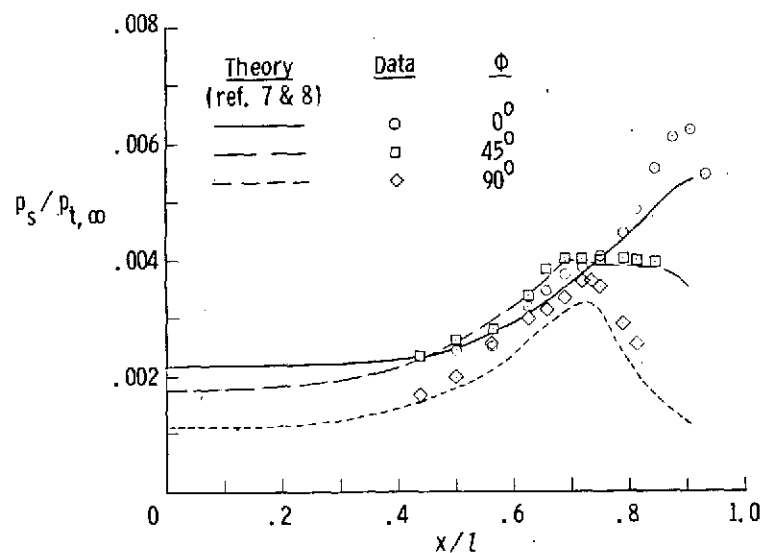
Figure 5.- Concluded.



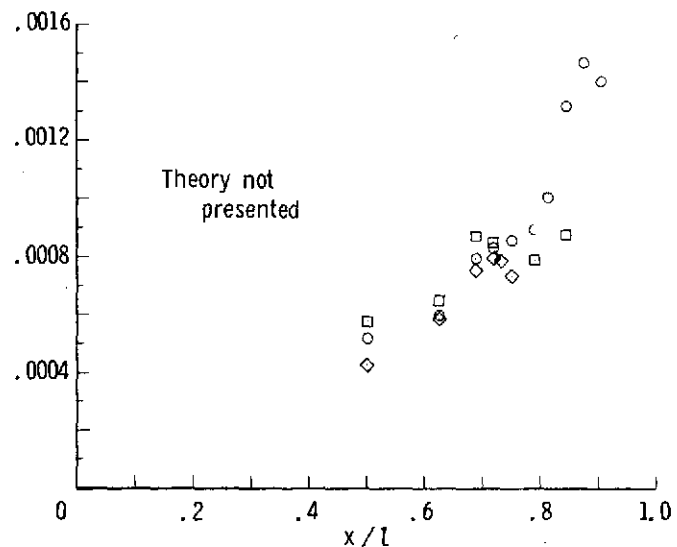
(a) $M_\infty = 6.0$; $\alpha = 0^\circ$.



(c) $M_\infty = 8.5$; $\alpha = 0^\circ$.

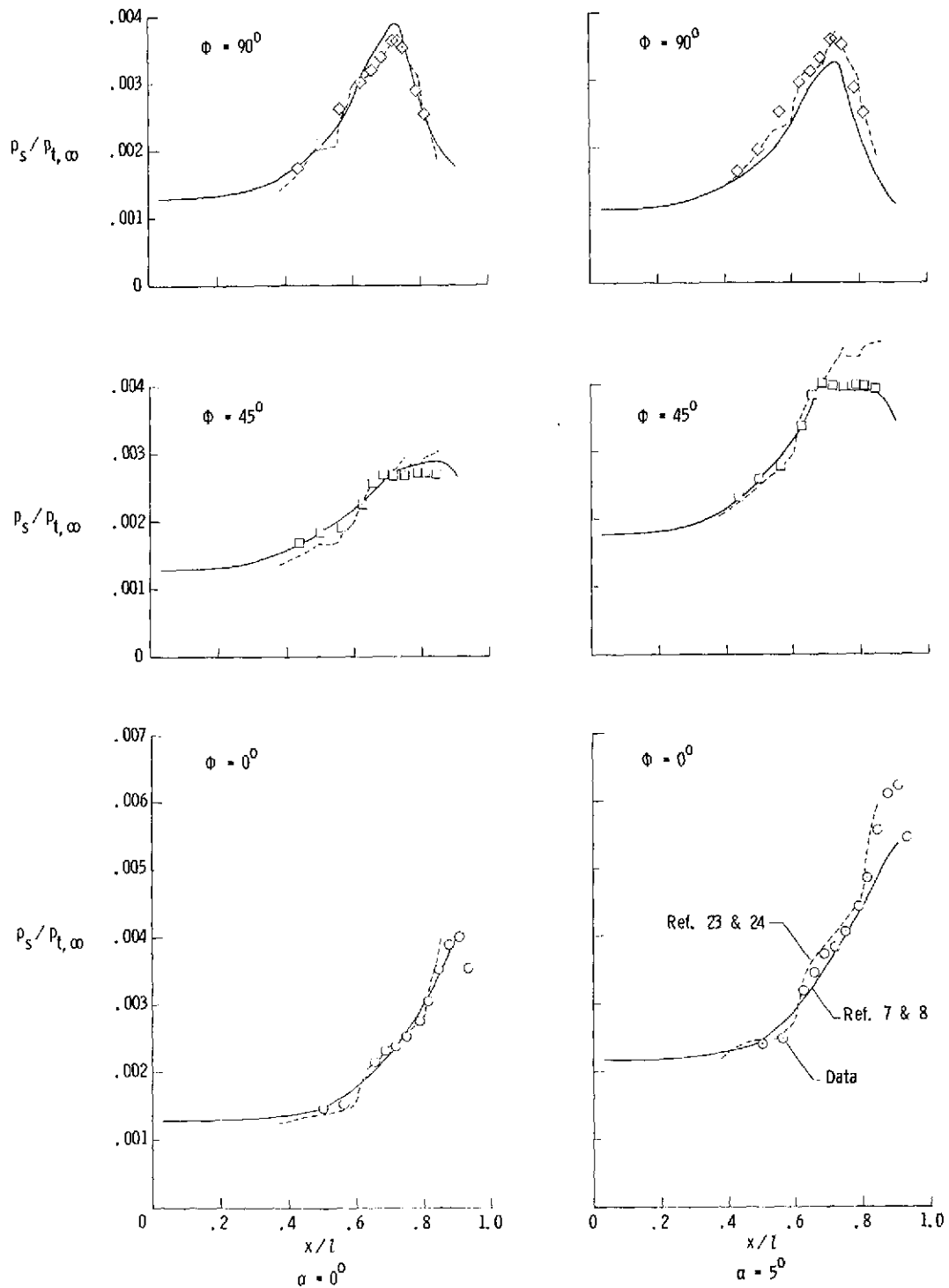


(b) $M_\infty = 6.0$; $\alpha = 5^\circ$.



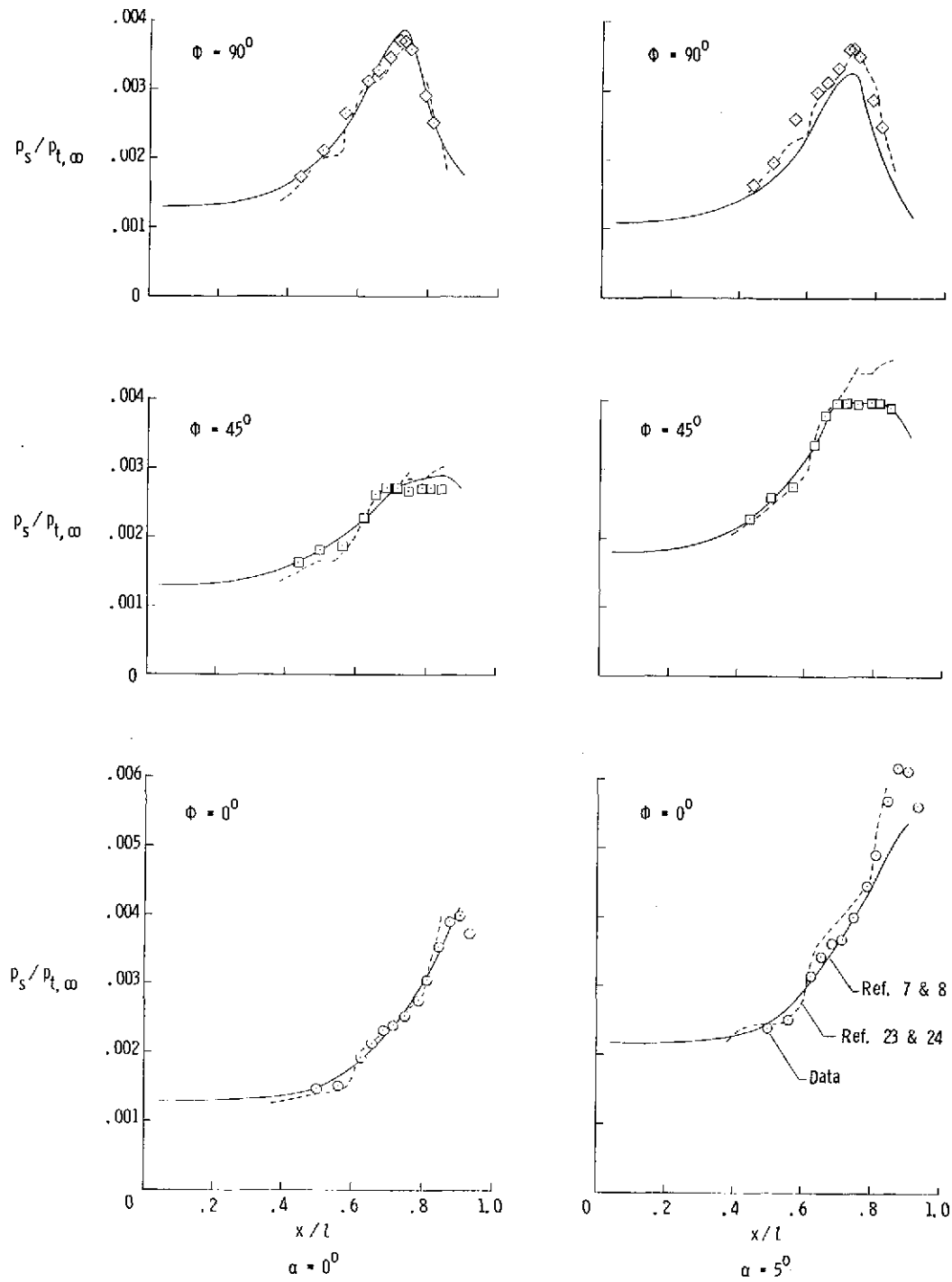
(d) $M_\infty = 8.5$; $\alpha = 5^\circ$.

Figure 6.- Static pressure distributions for three different radial planes; trips at $x/l = 0.188$; $\phi = 0^\circ$ (windward side).



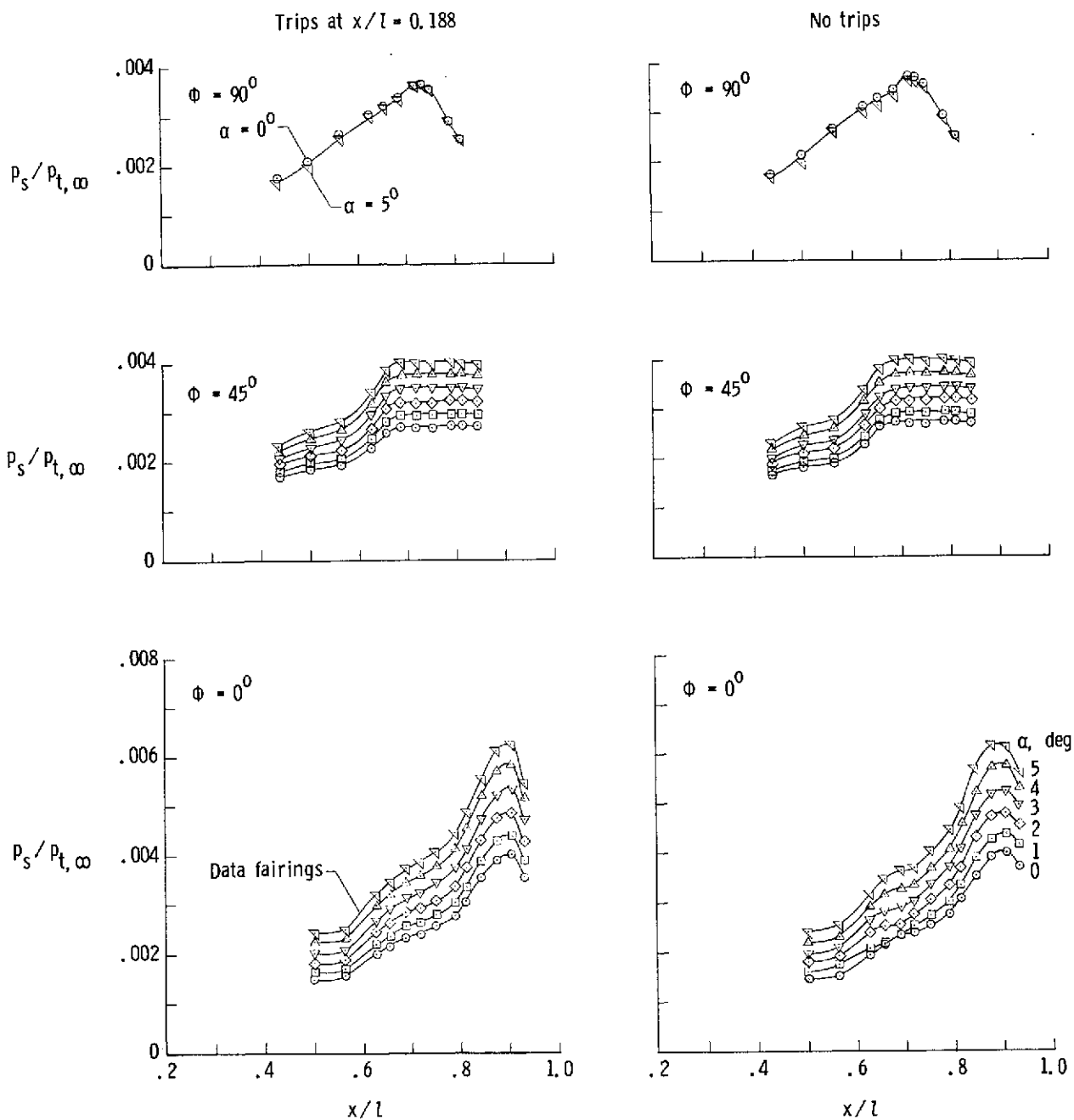
(a) With trips at $x/l = 0.188$.

Figure 7.- Experimental static pressure distributions compared with two different theoretical computation methods; $M_\infty = 6.0$; $\phi = 0^\circ$ (windward side).



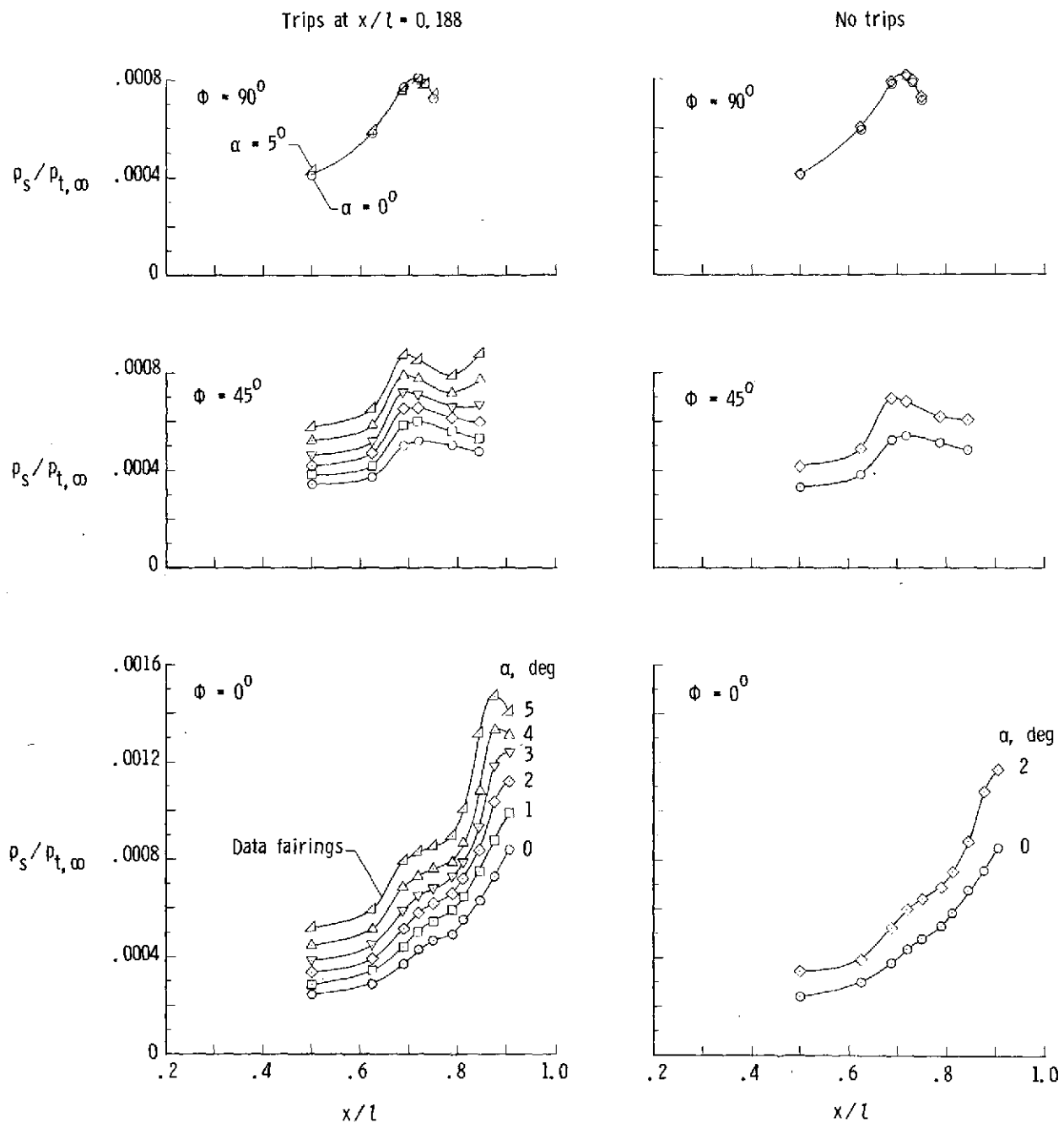
(b) Without trips.

Figure 7.- Concluded.



(a) $M_\infty = 6.0$.

Figure 8.- Experimental static pressure distributions at various model angles of attack with and without boundary-layer trips; $\phi = 0^\circ$ (windward side).



(b) $M_\infty = 8.5$.

Figure 8.- Concluded.

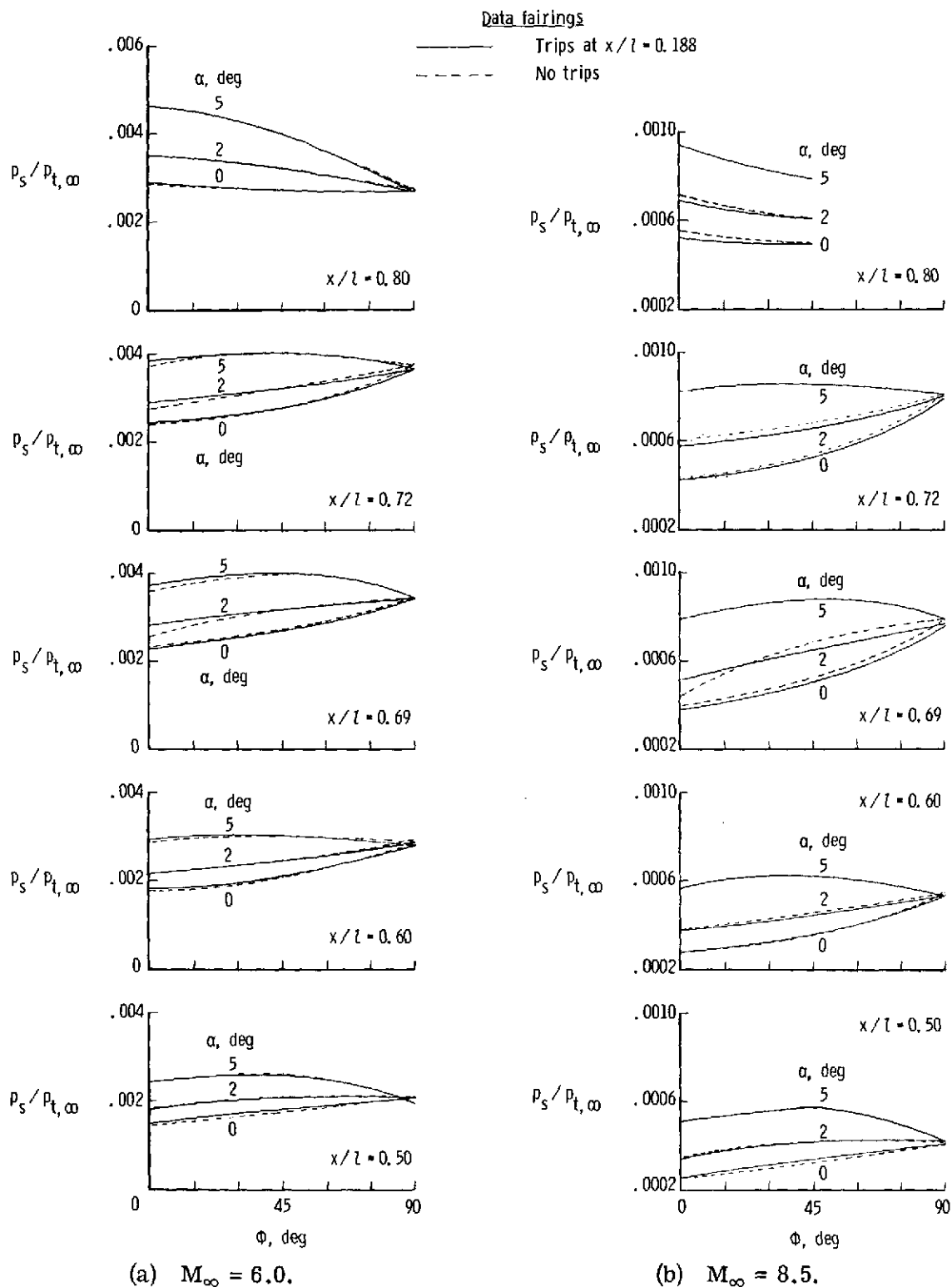
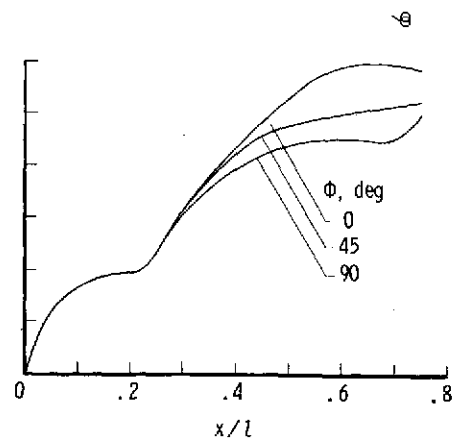
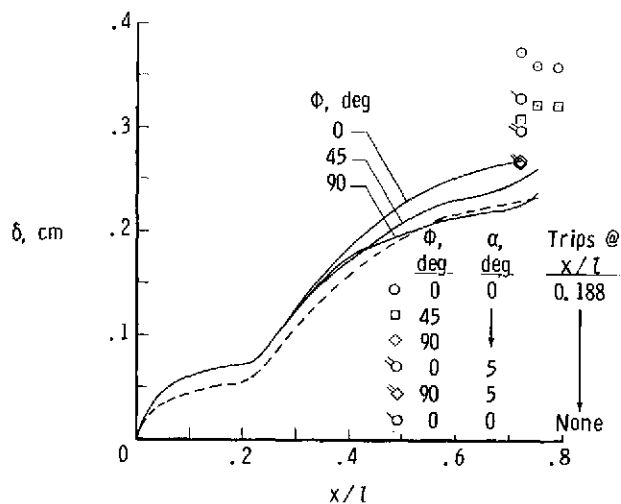
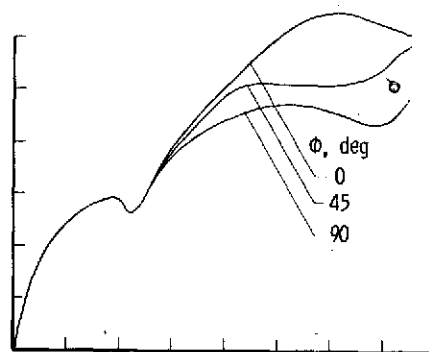
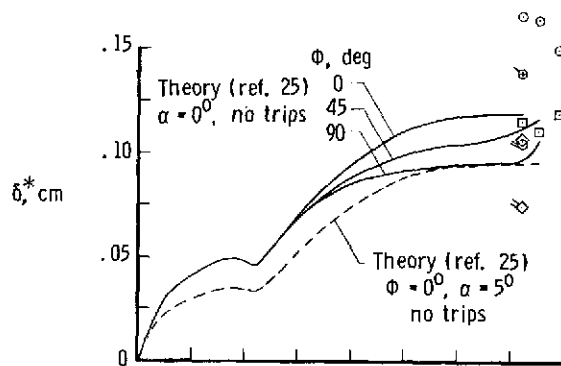
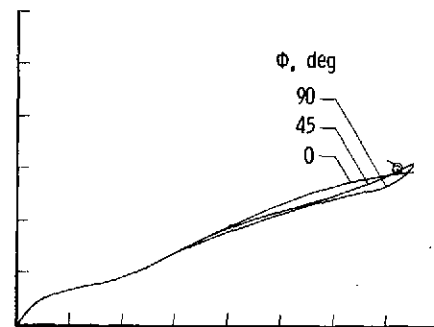
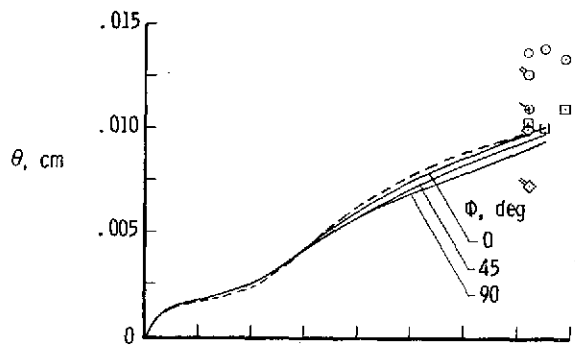


Figure 9.- Effect of angle of attack on lateral pressure gradients at various axial stations; $\phi = 0^\circ$ (windward side).



(a) $M_\infty = 6.0$.

(b) $M_\infty = 8.5$.

Figure 10.- Distribution of boundary-layer parameters; $\phi = 0^\circ$ (windward side).

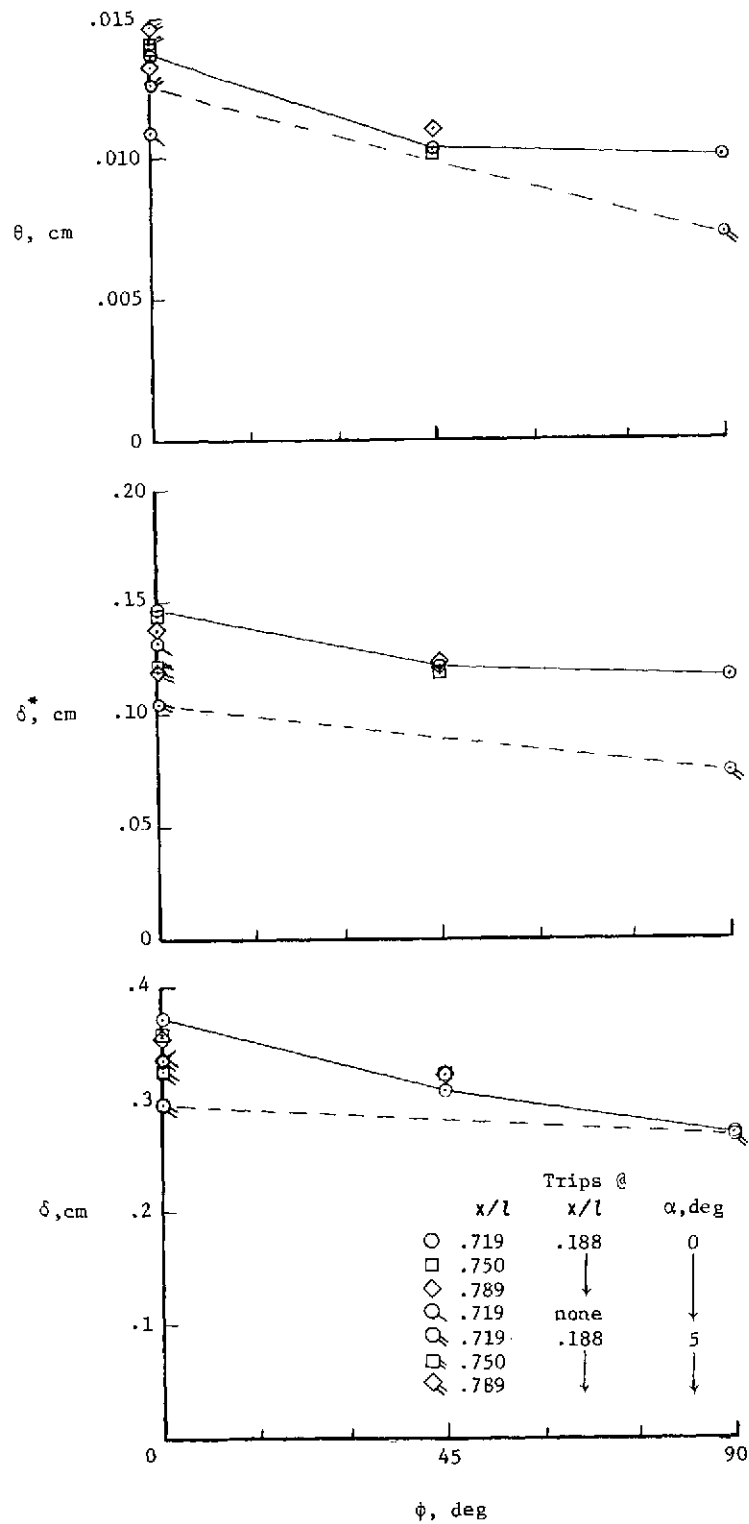


Figure 11.- Lateral distributions of experimental boundary-layer parameters; $M_\infty = 6.0$; $\phi = 0^\circ$ (windward side).

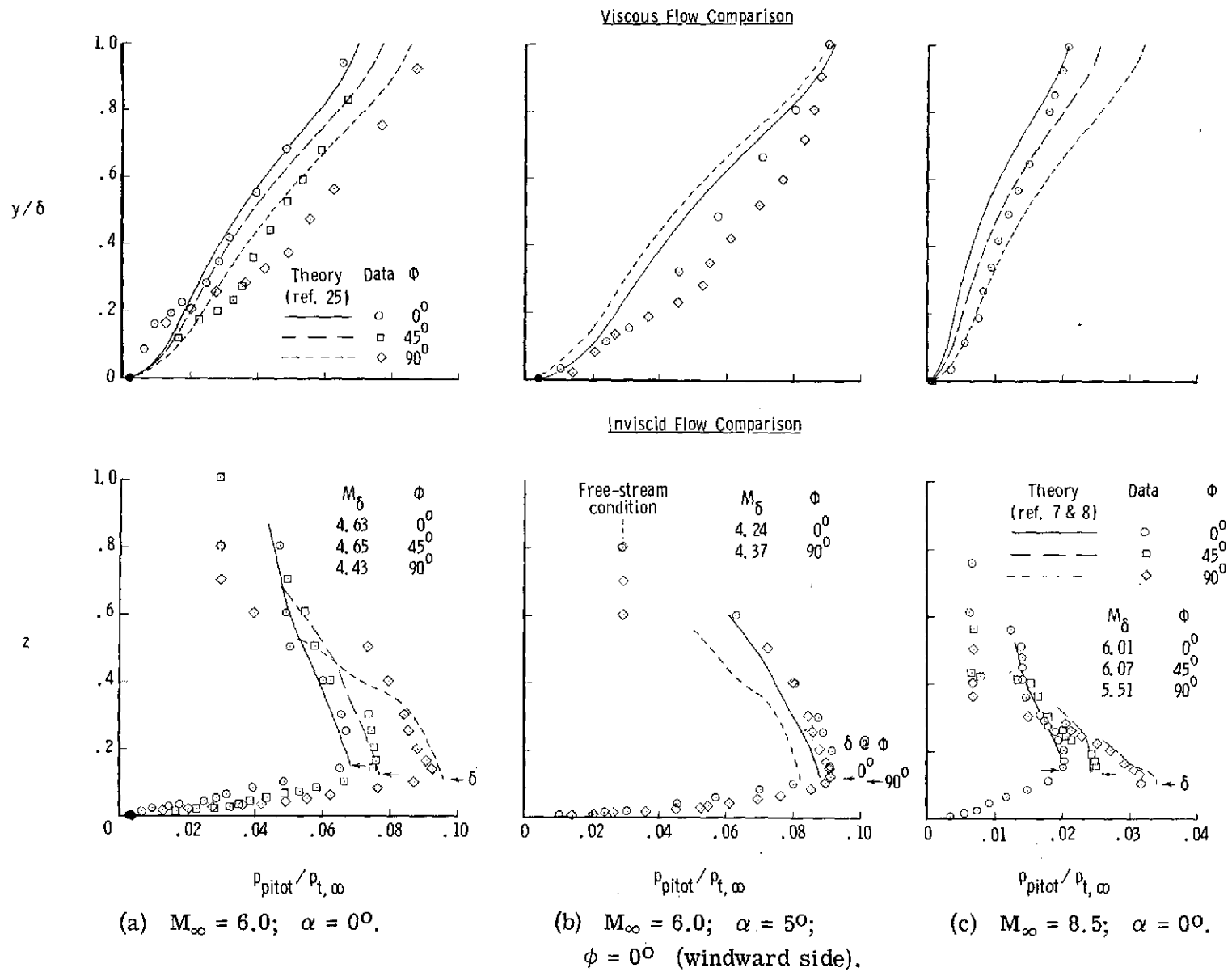


Figure 12.- Local pitot pressure profiles at various radial planes; $x/l = 0.719$; trips at $x/l = 0.188$.

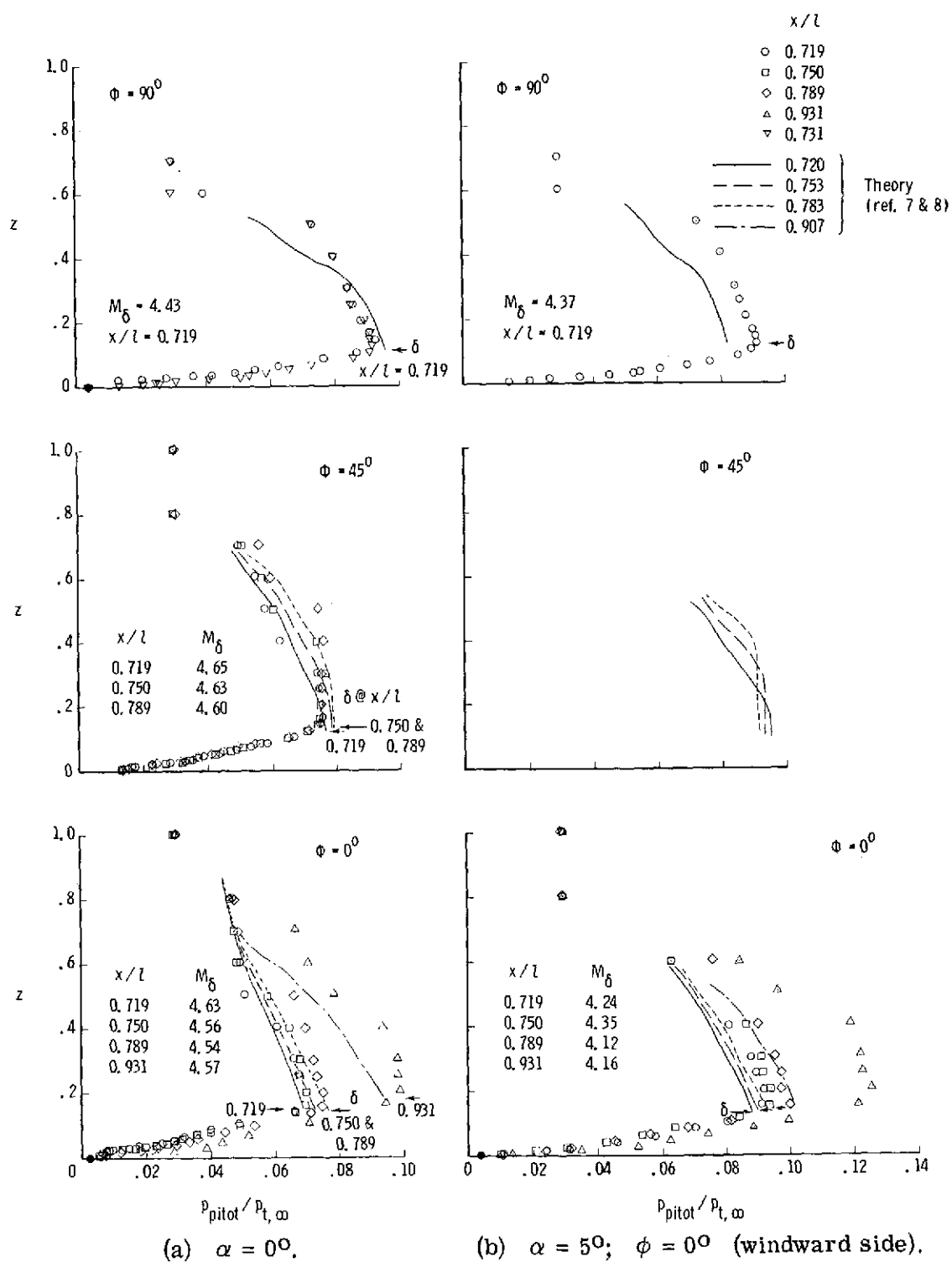


Figure 13.- Local pitot pressure profiles at various axial stations; $M_\infty = 6.0$; trips at $x/l = 0.188$.

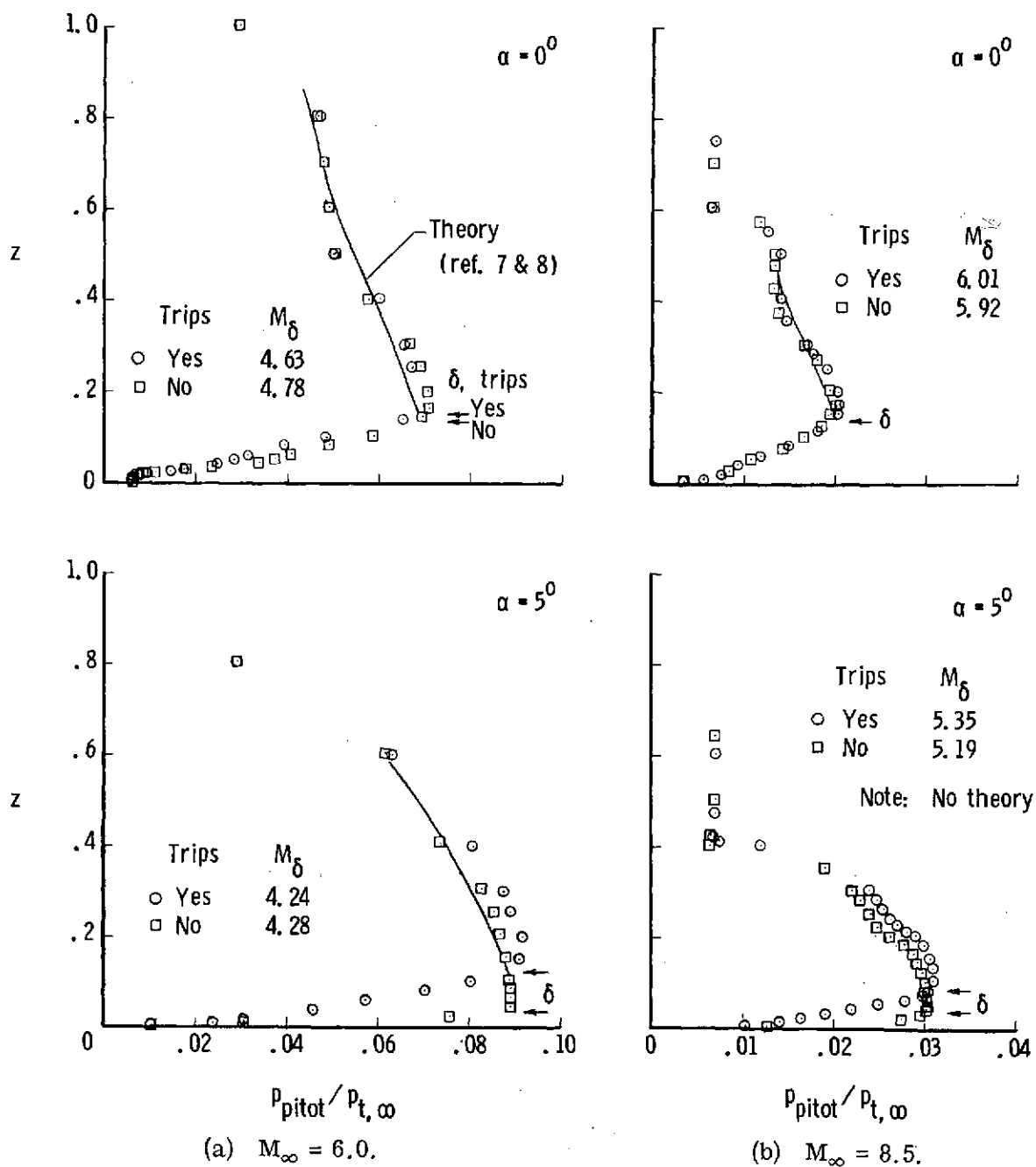
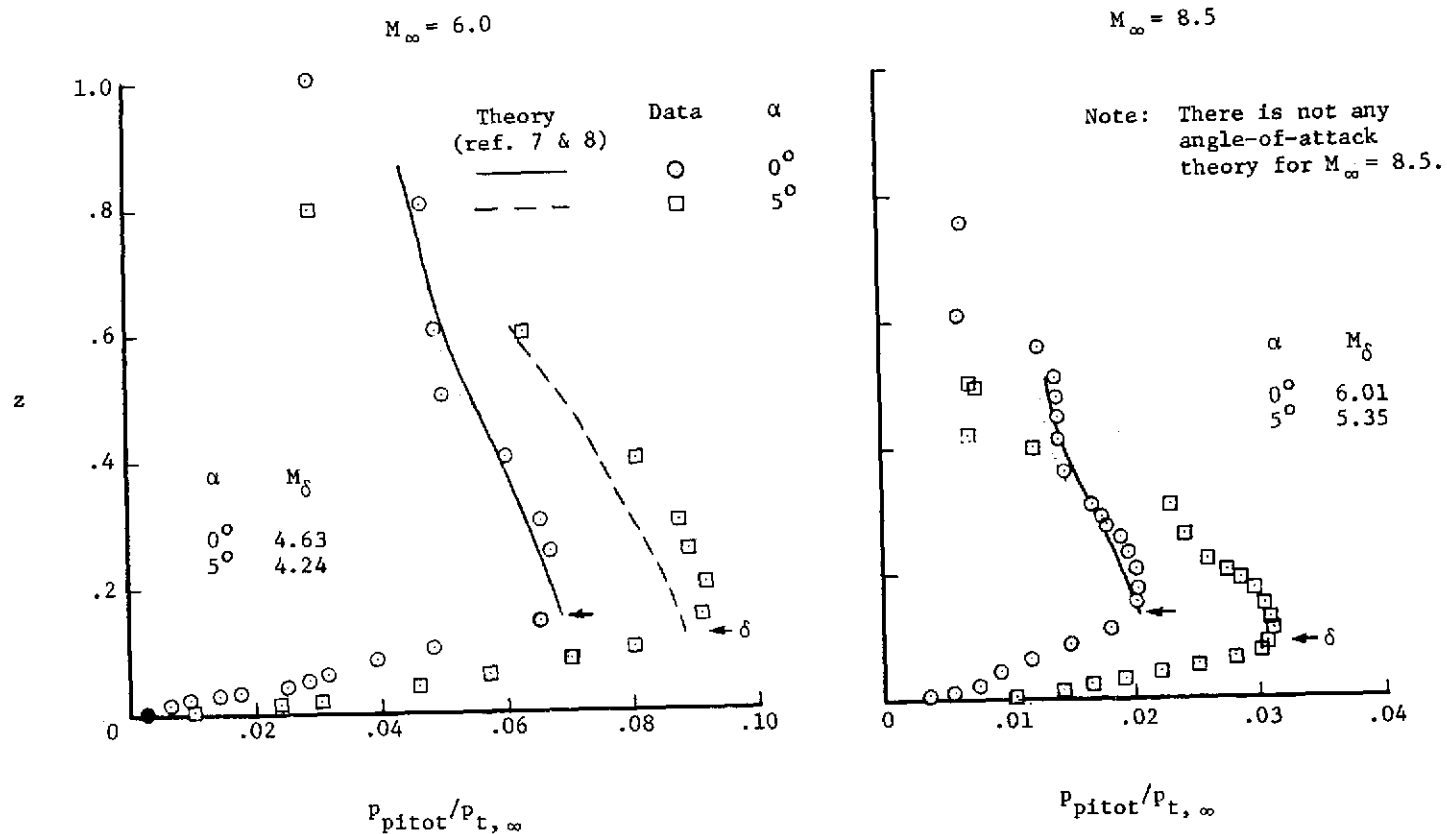
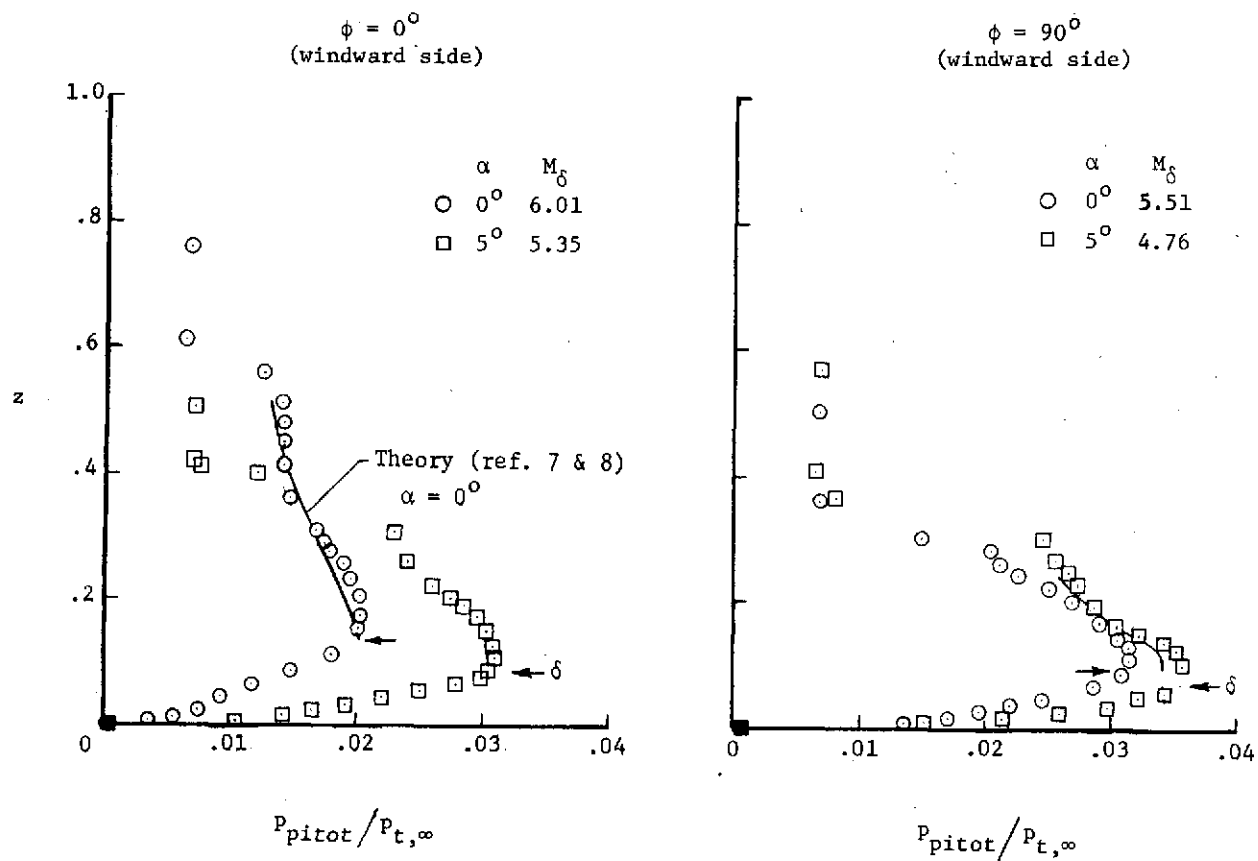


Figure 14.- Effect of boundary-layer trips on flow-field pitot pressures; $\phi = 0^\circ$; $x/l = 0.719$; trips at $x/l = 0.188$; $\phi = 0^\circ$ (windward side).



(a) $M_{\infty} = 6.0$ and 8.5 ; $\phi = 0^{\circ}$ (windward side).

Figure 15.- Effect of angle of attack on flow-field pitot pressures; trips at $x/l = 0.188$; $x/l = 0.719$.



(b) $M_\infty = 8.5$; $\phi = 0^\circ$ and 90° .

Figure 15.- Concluded.

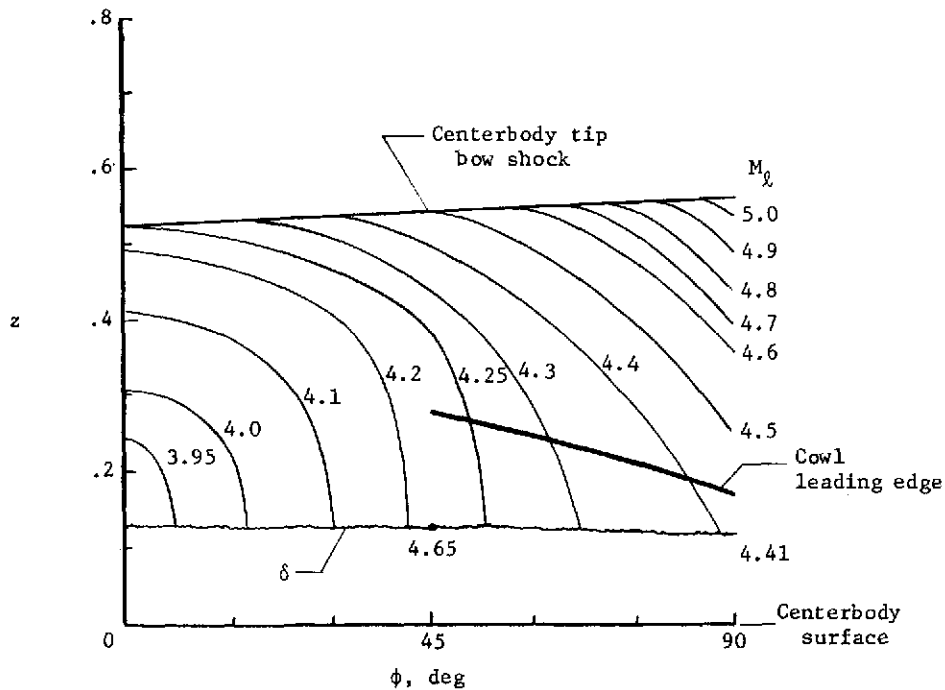
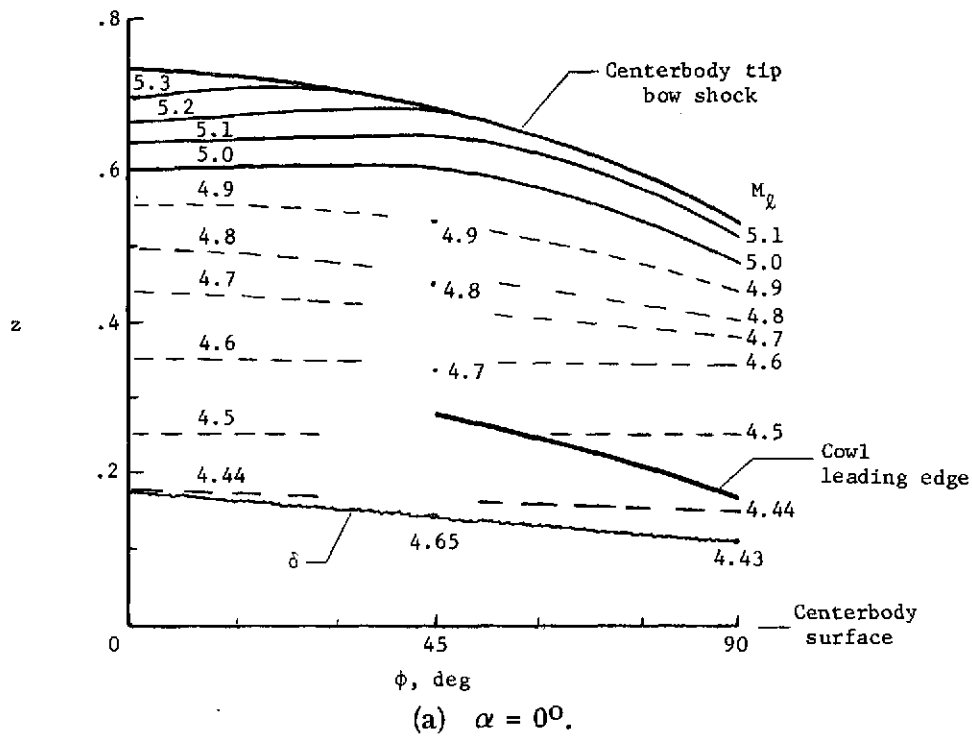
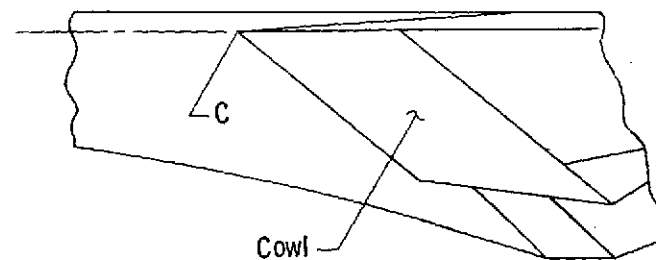
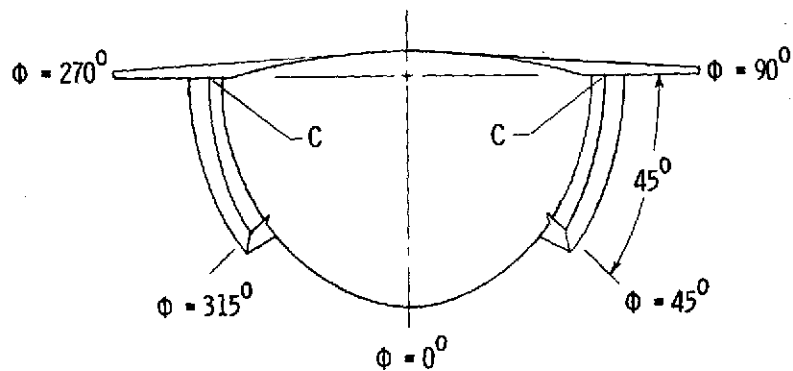
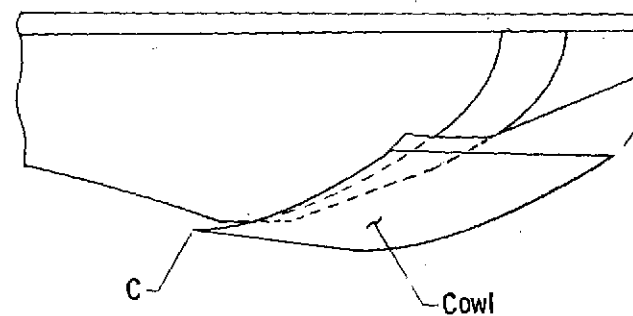
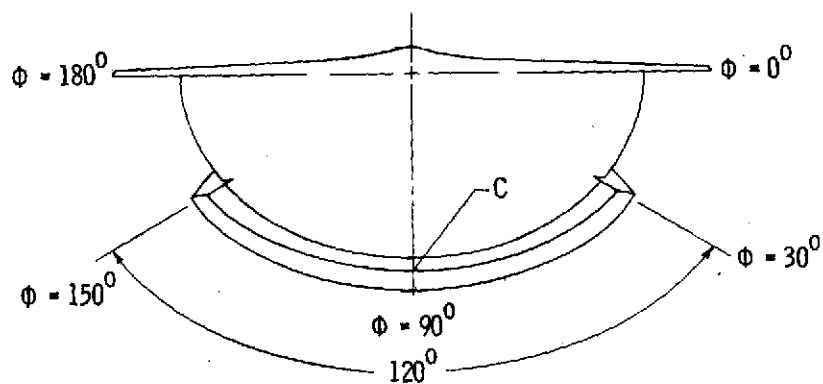


Figure 16.- Mach numbers in the vicinity of the inlet cowl leading edge; $M_\infty = 6.0$.

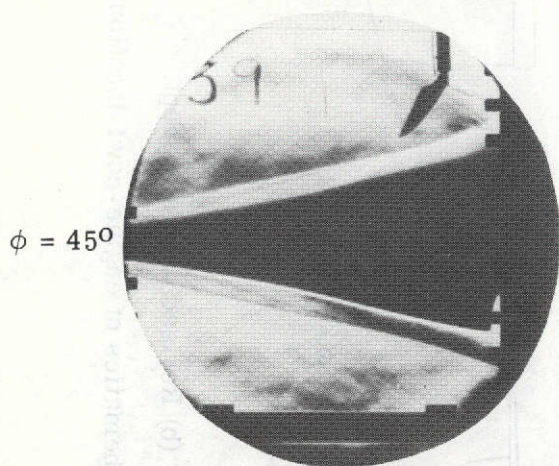
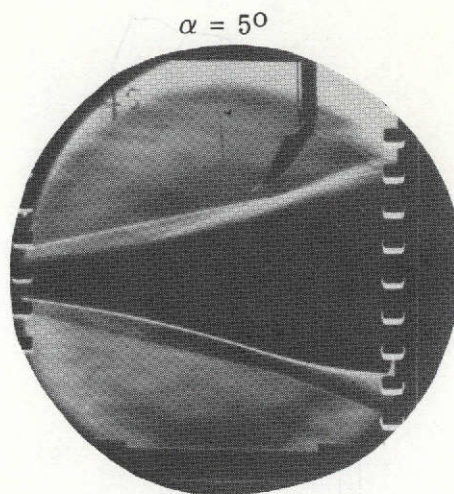
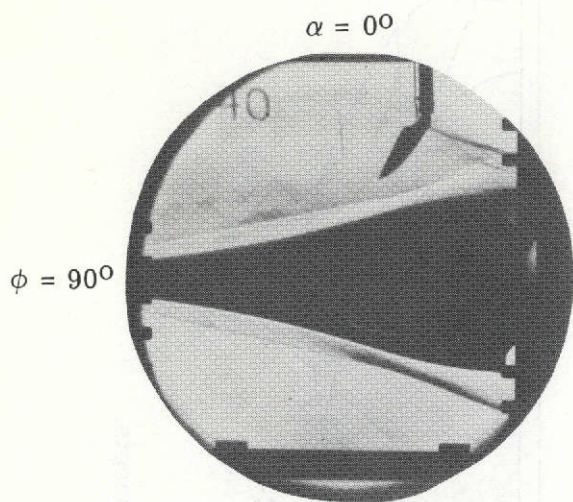


(a) Original design concept.

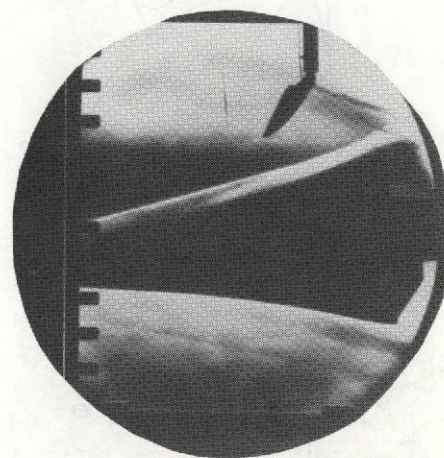
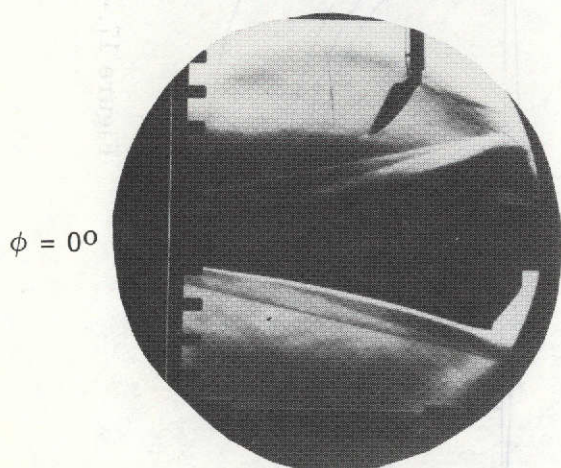


(b) Revised design concept.

Figure 17.- Schematics of engine-cowl-location concepts.

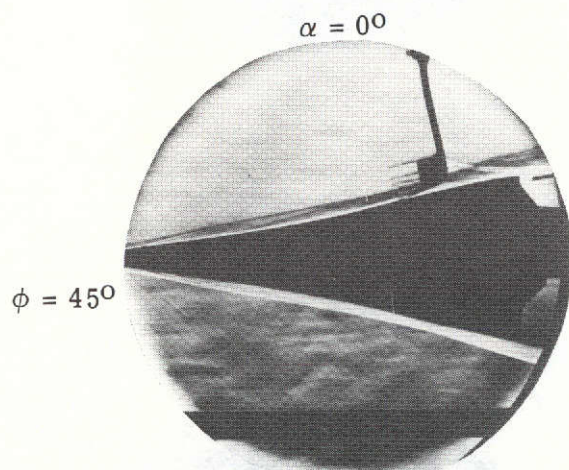
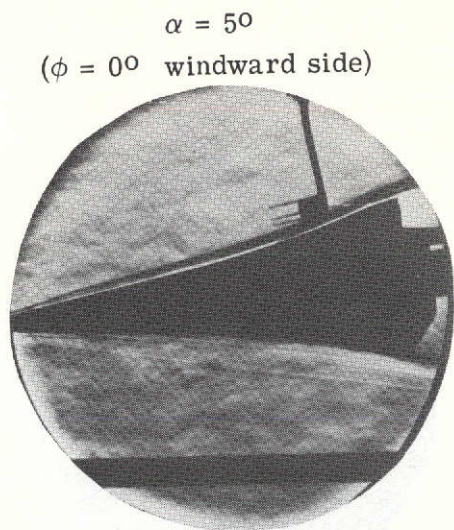
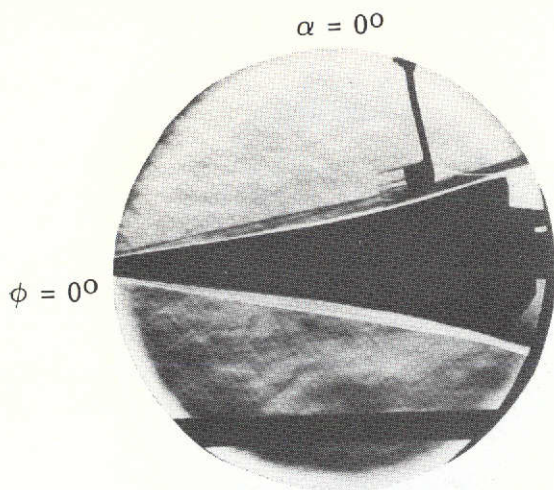


REPRODUCIBILITY OF THE
ORIGINAL PAGE IS POOR

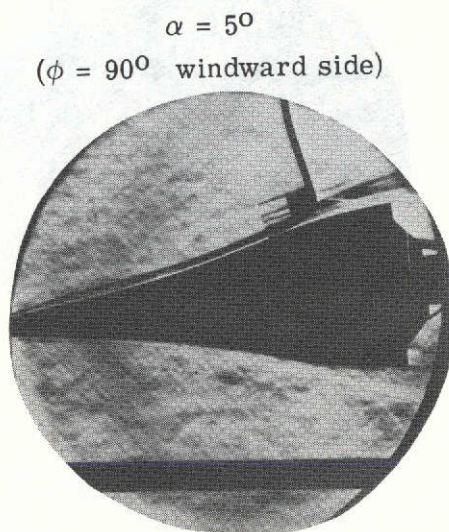
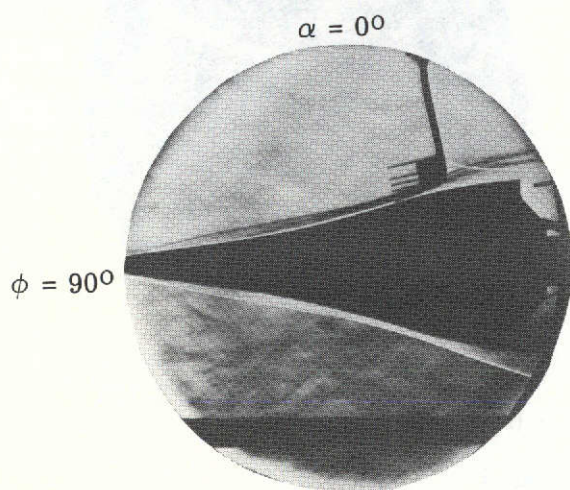


(a) Mach 6.0 with trips at $x/l = 0.188$; $\phi = 0^\circ$ (windward side). L-75-123

Figure 18.- Schlieren photographs.



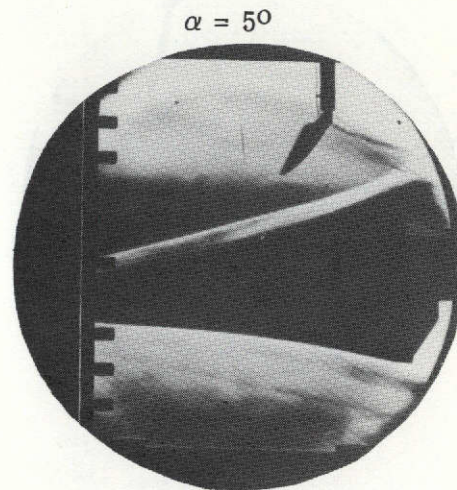
REPRODUCIBILITY OF THE
ORIGINAL PAGE IS POOR



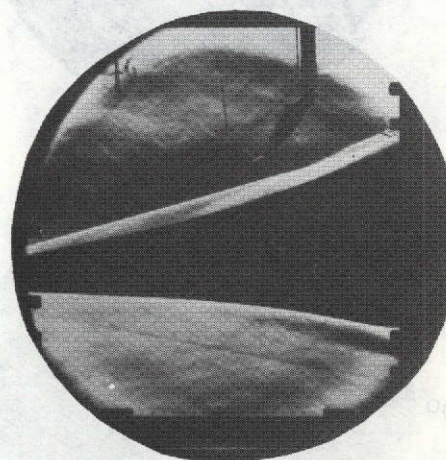
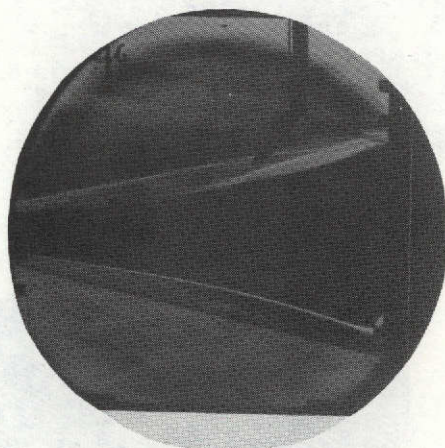
L-75-124

(b) Mach 8.5 with trips at $x/l = 0.188$.

Figure 18.- Continued.



With trips at $x/l = 0.188$.

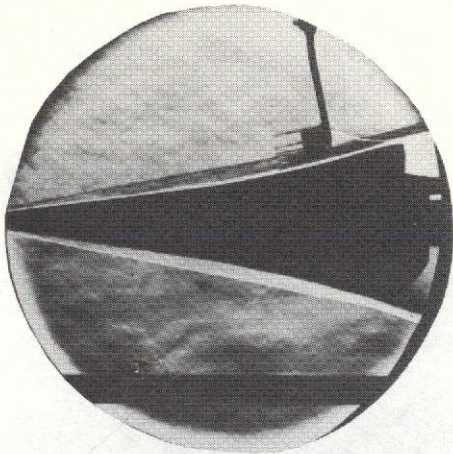


No trips

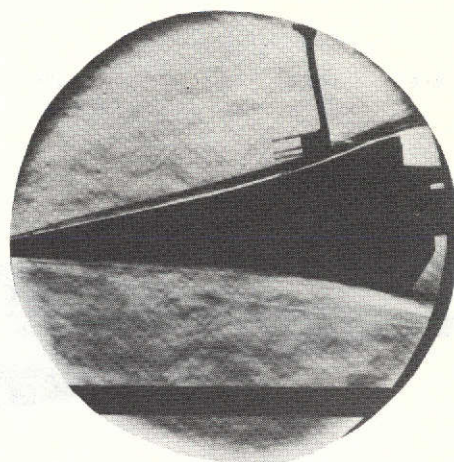
(c) Effect of trips; $M_\infty = 6.0$; $\phi = 0^\circ$ (windward side). L-75-125

Figure 18. - Continued.

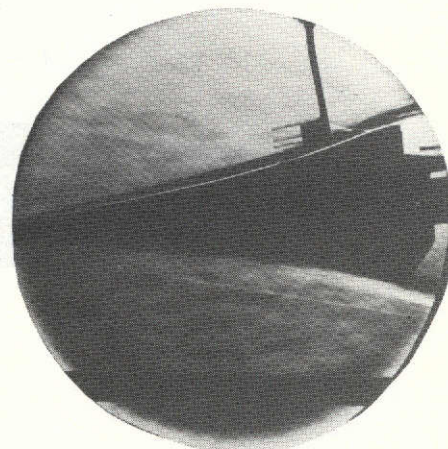
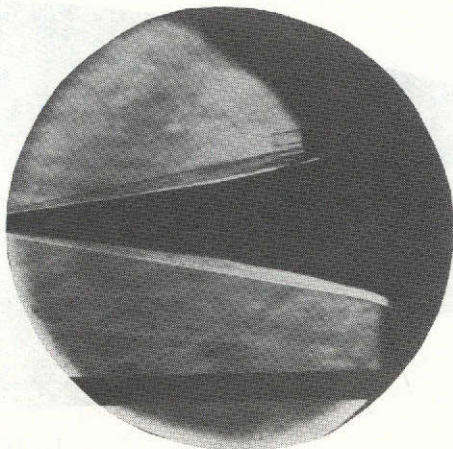
$\alpha = 0^\circ$



$\alpha = 5^\circ$



With trips at $x/l = 0.188$

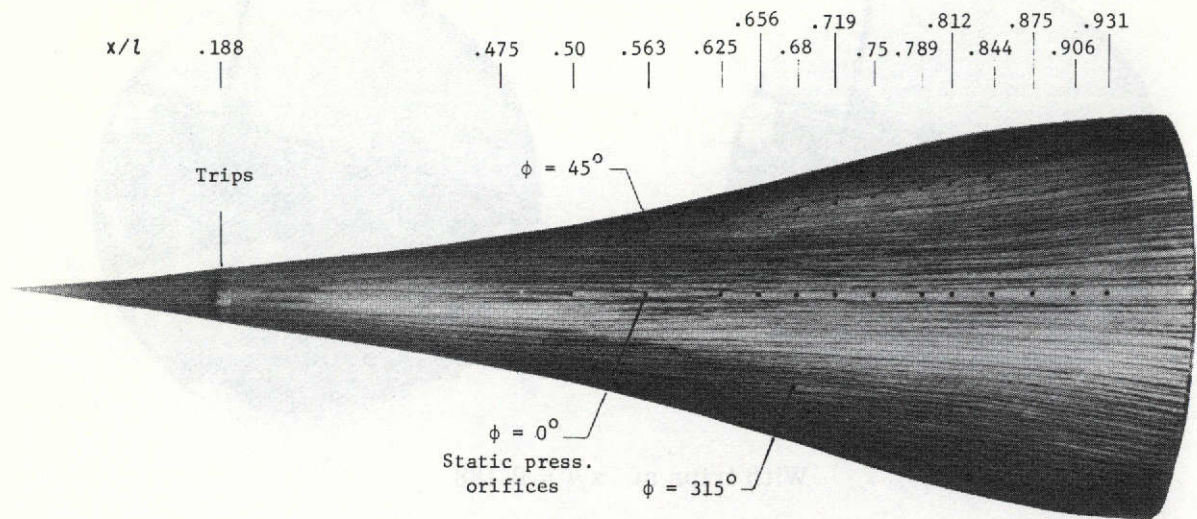


No trips

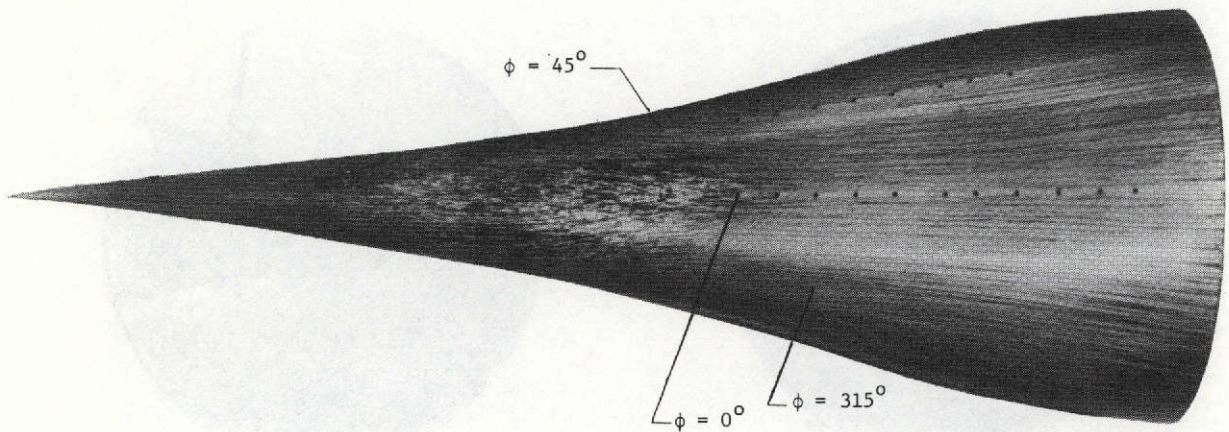
L-75-126

(d) Effect of trips; $M_\infty = 8.5$; $\phi = 0^\circ$ (windward side).

Figure 18.- Concluded.



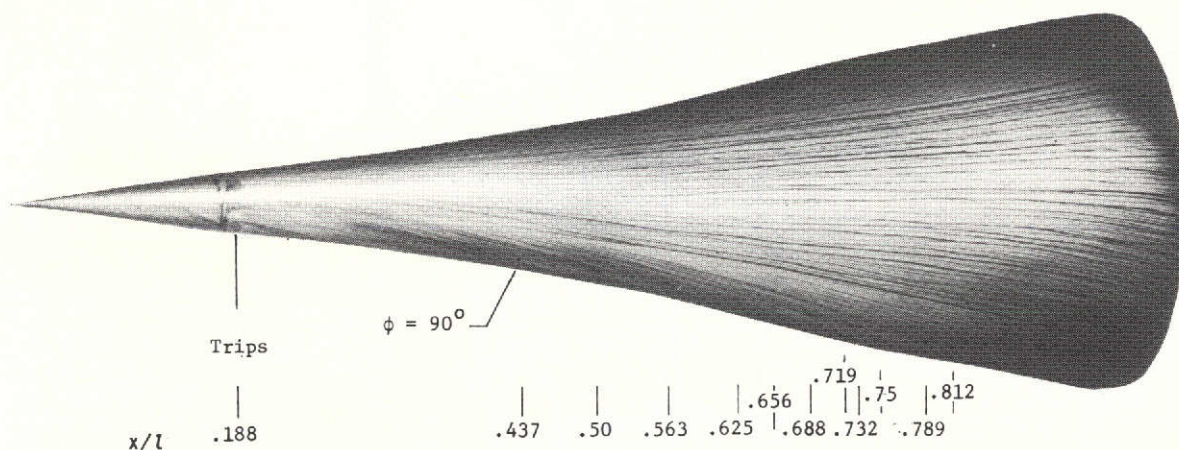
(a) With boundary-layer trips.



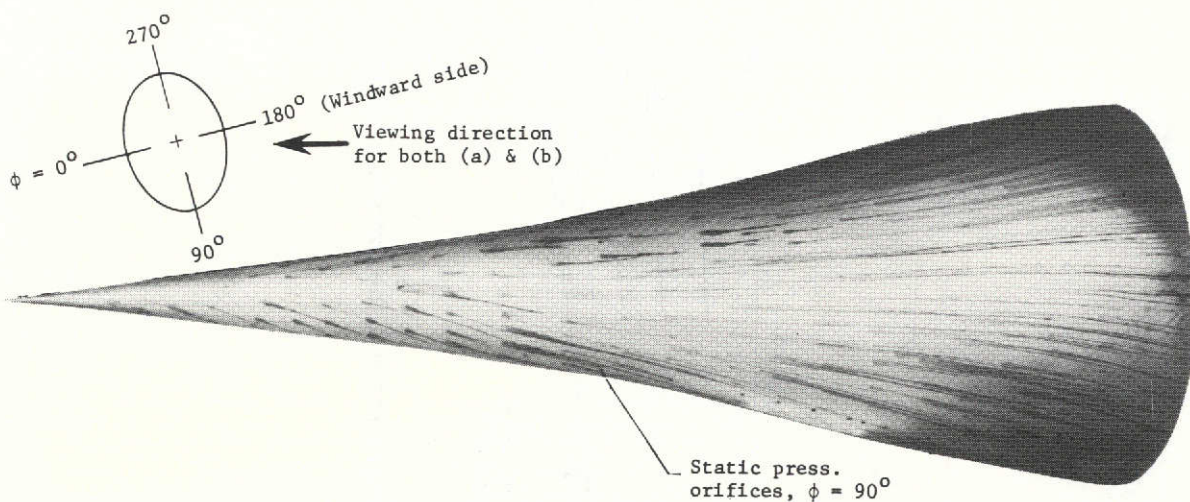
L-75-127

(b) No boundary-layer trips.

Figure 19.- Photographic results of oil-streak tests; $M_\infty = 6.0$; $\alpha = 0^\circ$.



(a) With boundary-layer trips.



L-75-128

(b) No boundary-layer trips.

Figure 20.- Photographic results of oil-streak tests; $M_\infty = 6.0$; $\alpha = 5^\circ$; $\phi = 180^\circ$ (windward side); (Body is symmetric, therefore the same as $\phi = 0^\circ$ (windward side)).

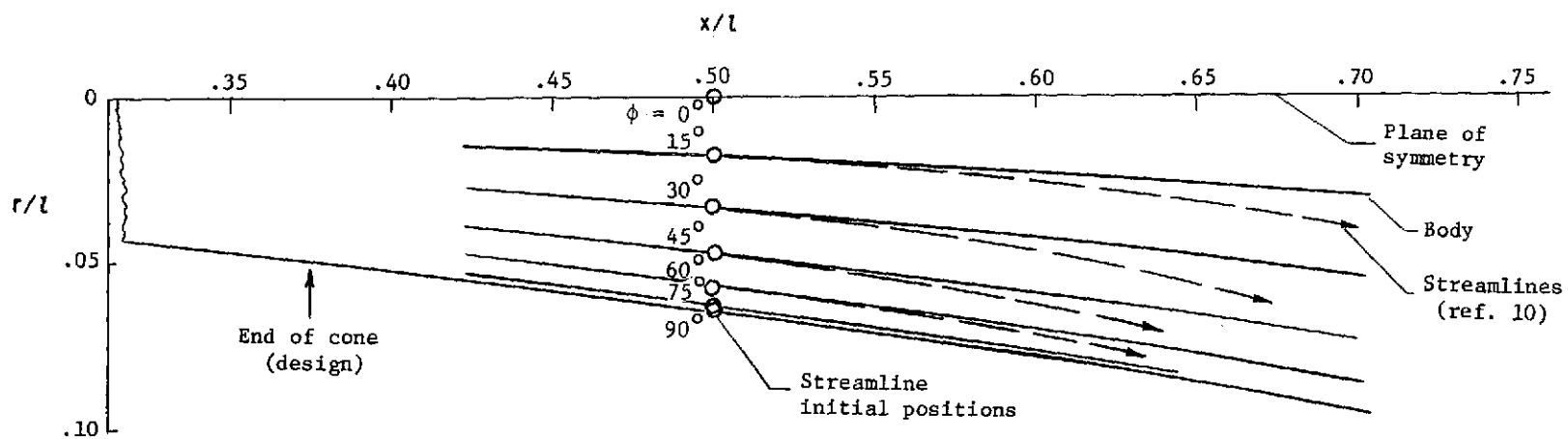


Figure 21.- Surface streamline patterns; planform view; $M_\infty = 6.0$; $\alpha = 3^\circ$; $\phi = 0^\circ$ (windward side).